Satellite Observations of Stratospheric Carbonyl Fluoride

by

Jeremy J. Harrison[1], Martyn P. Chipperfield[2], Anu Dudhia[3], Shaomin Cai[3], Sandip Dhomse[2], Christopher D. Boone[4], and Peter F. Bernath[1,5]

[1]*Department of Chemistry, University of York, Heslington, York, YO10 5DD, United Kingdom.*

[2]*Institute for Climate and Atmospheric Science, School of Earth and Environment, University of Leeds, Leeds, LS2 9JT, United Kingdom.*

[3]*Atmospheric, Oceanic and Planetary Physics, Clarendon Laboratory, University of Oxford, Parks Road, Oxford, OX1 3PU, United Kingdom.*

[4]*Department of Chemistry, University of Waterloo, 200 University Avenue West, Ontario N2L 3G1, Canada.*

[5]*Department of Chemistry and Biochemistry, Old Dominion University, Norfolk, Virginia 23529, United States of America.*

Number of pages   = 37

Number of tables   = 6

Number of figures = 14

Address for correspondence:

            Dr. Jeremy J. Harrison,

            Department of Chemistry,

            University of York,

            Heslington,

            York YO10 5DD,

            United Kingdom

Tel: (44)-1904-324589

Fax: (44)-1904-432516

e-mail: jeremy.harrison@york.ac.uk

Abstract

35

36   The vast majority of emissions of fluorine-containing molecules are anthropogenic

37   in nature, e.g. chlorofluorocarbons (CFCs), hydrochlorofluorocarbons (HCFCs), and

38   hydrofluorocarbons (HFCs). These molecules slowly degrade in the atmosphere leading to

39   the formation of HF, COF_2, and COClF, which are the main fluorine-containing species in

40   the stratosphere. Ultimately both COF_2 and COClF further degrade to form HF, an almost

41   permanent reservoir of stratospheric fluorine due to its extreme stability. Carbonyl fluoride

42   (COF_2) is the second most abundant stratospheric 'inorganic' fluorine reservoir with main

43   sources being the atmospheric degradation of CFC-12 (CCl_2F_2), HCFC-22 (CHF_2Cl), and

44   CFC-113 ($CF_2ClCFCl_2$).

45   This work reports the first global distributions of carbonyl fluoride in the Earth's

46   atmosphere using infrared satellite remote-sensing measurements by the Atmospheric

47   Chemistry Experiment Fourier transform spectrometer (ACE-FTS), which has been

48   recording atmospheric spectra since 2004, and the Michelson Interferometer for Passive

49   Atmospheric Sounding (MIPAS) instrument, which has recorded thermal emission

50   atmospheric spectra between 2002 and 2012. The observations reveal a high degree of

51   seasonal and latitudinal variability over the course of a year. These have been compared with

52   the output of SLIMCAT, a state-of-the-art three-dimensional chemical transport model. In

53   general the observations agree well with each other, although MIPAS is biased high by as

54   much as ~ 30 %, and compare well with SLIMCAT.

55   Between January 2004 and September 2010 COF_2 grew most rapidly at altitudes

56   above ~25 km in the southern latitudes and at altitudes below ~25 km in the northern

57   latitudes, whereas it declined most rapidly in the tropics. These variations are attributed to

58   changes in stratospheric dynamics over the observation period. The overall COF_2 global

59   trend over this period is calculated as 0.85 ± 0.34 %/year (MIPAS), 0.30 ± 0.44 %/year

60   (ACE), and 0.88 %/year (SLIMCAT).

61

1. Introduction

Although small quantities of fluorine-containing molecules are emitted into the atmosphere from natural sources, e.g. volcanic and hydrothermal emissions (Gribble, 2002), the vast majority of emissions are anthropogenic in nature, e.g. chlorofluorocarbons (CFCs), hydrochlorofluorocarbons (HCFCs), and hydrofluorocarbons (HFCs). Most fluorine in the troposphere is present in its emitted 'organic' form due to these molecules having typical lifetimes of a decade or longer, however photolysis in the stratosphere, which liberates fluorine atoms that react with methane, water or molecular hydrogen, result in the formation of the 'inorganic' product hydrogen fluoride, HF. At the top of the stratosphere (~50 km altitude), ~ 75% of the total available fluorine is present as HF (Brown et al., 2014). Due to its extreme stability, HF is an almost permanent reservoir of stratospheric fluorine, meaning the atmospheric concentrations of F and FO, necessary for an ozone-destroying catalytic cycle, are very small (Tressaud, 2006). For this reason fluorine does not cause any significant ozone loss. HF is removed from the stratosphere by slow transport to, and rainout in, the troposphere, or by upward transport to the mesosphere, where it is destroyed by photolysis (Duchatelet et al., 2010). The recent stratospheric fluorine inventory for 2004–2009 (Brown et al., 2014) indicates a year-on-year increase of HF and total fluorine.

The second most abundant stratospheric 'inorganic' fluorine reservoir is carbonyl fluoride (COF_2), largely due to its slow photolysis. Recent studies indicate that its atmospheric abundance is increasing (Duchatelet et al., 2009; Brown et al., 2011). The main sources of COF_2 are the atmospheric degradation of CFC-12 (CCl_2F_2) and CFC-113 ($CF_2ClCFCl_2$), which are both now banned under the Montreal Protocol, and HCFC-22 (CHF_2Cl), the most abundant HCFC and classed as a transitional substitute under the Montreal Protocol. Although the amounts of CFC-12 and CFC-113 in the atmosphere are now slowly decreasing, HCFC-22 is still on the increase. For the two most abundant source molecules, CFC-12 and HCFC-22, the atmospheric degradation proceeds by their initial breakdown into CF_2Cl (Tressaud, 2006),

$$CF_2Cl_2 + h\nu \rightarrow CF_2Cl + Cl$$
$$CHF_2Cl + OH \rightarrow CF_2Cl + H_2O \quad\quad (R1)$$

followed by

$$CF_2Cl + O_2 + M \rightarrow CF_2ClO_2 + M$$

3

96 $$CF_2ClO_2 + NO \rightarrow CF_2ClO + NO_2$$

97 $$CF_2ClO + O_2 \rightarrow COF_2 + ClO_2. \tag{R2}$$
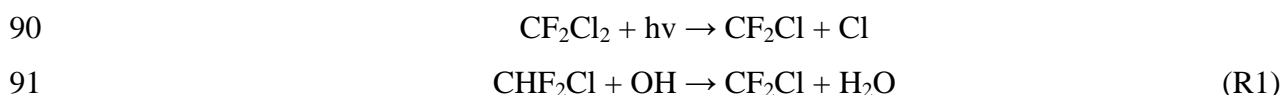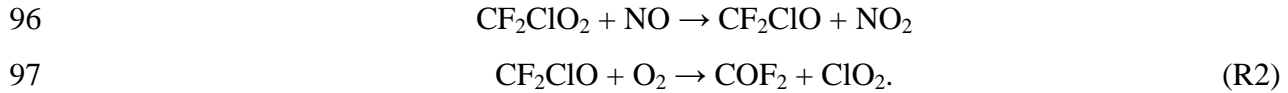
98

99 For CFC-113 and more minor sources such as HFCs (e.g. HFC-134a, HFC-152a), the

100 reaction scheme is similar.

101   COF_2 volume mixing ratios (VMRs) slowly increase with altitude up to the middle

102 of the stratosphere, above which they decrease as photolysis of COF_2 becomes more

103 efficient, leading to the formation of fluorine atoms,

104

105 $$COF_2 + h\nu \rightarrow FCO + F$$

106 $$FCO + O_2 + M \rightarrow FC(O)O_2 + M$$

107 $$FC(O)O_2 + NO \rightarrow FCO_2 + NO_2$$

108 $$FCO_2 + h\nu \rightarrow F + CO_2. \tag{R3}$$
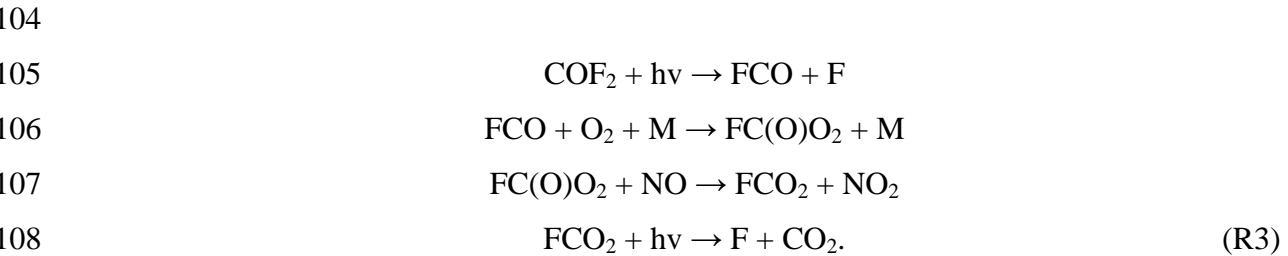
109

110 As mentioned earlier, these F atoms react with CH_4, H_2O or H_2 to form HF.

111   Monitoring COF_2 as part of the atmospheric fluorine family is important to close the

112 fluorine budget, particularly as the majority of atmospheric fluorine arises from

113 anthropogenic emissions. Previously, vertical profiles of COF_2 in the atmosphere have been

114 determined from measurements taken by the Atmospheric Trace MOlecule Spectrometry

115 Experiment (ATMOS) instrument which flew four times on NASA space shuttles between

116 1985 and 1994 (Rinsland et al., 1986; Zander et al., 1994). Additionally, there have been

117 several studies into the seasonal variability of COF_2 columns above Jungfraujoch using

118 ground-based Fourier transform infrared (FTIR) solar observations (Mélen et al., 1998;

119 Duchatelet et al., 2009). The use of satellite remote-sensing techniques allows the

120 measurement of COF_2 atmospheric abundances with global coverage, and the investigation

121 more fully of COF_2 trends, and seasonal and latitudinal variability. This work presents the

122 first global distributions of COF_2 using data from two satellite limb instruments: the

123 Atmospheric Chemistry Experiment Fourier transform spectrometer (ACE-FTS), onboard

124 SCISAT (SCIentific SATellite), which has been recording atmospheric spectra since 2004,

125 and the Michelson Interferometer for Passive Atmospheric Sounding (MIPAS) instrument

126 (Fischer et al., 2008) onboard the ENVIronmental SATellite (Envisat), which has recorded

127 thermal emission atmospheric spectra between 2002 and 2012. This work also provides

128 comparisons of these observations with the output of SLIMCAT, a state-of-the-art three-

129 dimensional (3D) chemical transport model (CTM). Models have not been tested against

4

130 COF$_2$ observations in detail before; in fact, many standard stratospheric models do not even
131 include fluorine chemistry. Model comparisons with global datasets are essential to test how
132 well COF$_2$ chemistry is understood.

133   In Sections 2 and 3 of this paper, full details of the ACE and MIPAS retrieval
134 schemes and associated errors are presented. ACE and MIPAS zonal means and profiles are
135 compared in Section 4, with both sets of observations compared with SLIMCAT in Section
136 5. Finally, trends in COF$_2$ VMRs between 2004 and 2010 are calculated and discussed in
137 Section 6.

138

139

140 **2. Retrieval of carbonyl fluoride**

141 **2.1. ACE-FTS spectra**

142   The ACE-FTS instrument, which covers the spectral region 750 to 4400 cm^{-1} with a
143 maximum optical path difference (MOPD) of 25 cm and a resolution of 0.02 cm^{-1} (using the
144 definition of 0.5/MOPD throughout), uses the sun as a source of infrared radiation to record
145 limb transmission through the Earth's atmosphere during sunrise and sunset ('solar
146 occultation'). Transmittance spectra are obtained by ratioing against exo-atmospheric 'high
147 sun' spectra measured each orbit. These spectra, with high signal-to-noise ratios, are
148 recorded through long atmospheric limb paths (~300 km effective length), thus providing a
149 low detection threshold for trace species. ACE has an excellent vertical resolution of about
150 ~3 km (Clerbaux et al., 2005) and can measure up to 30 occultations per day, with each
151 occultation sampling the atmosphere from 150 km down to the cloud tops (or 5 km in the
152 absence of clouds). The locations of ACE occultations are dictated by the low Earth circular
153 orbit of SCISAT and the relative position of the sun. Over the course of a year, the ACE-
154 FTS records atmospheric spectra over a large portion of the globe (Bernath et al., 2005).

155   The atmospheric pressure and temperature profiles, the tangent heights of the
156 measurements, and the carbonyl fluoride VMRs were taken from the version 3.0 processing
157 of the ACE-FTS data (Boone et al., 2005; 2013). Vertical profiles of trace gases (along with
158 temperature and pressure) are derived from the recorded transmittance spectra via an iterative
159 Levenberg-Marquardt nonlinear least-squares global fit to the selected spectral region(s) for
160 all measurements within the altitude range of interest, according to the equation

161

$$\mathbf{x}_{i+1} = \mathbf{x}_i + \left(\mathbf{K}^T \mathbf{S}_y^{-1} \mathbf{K} + \lambda \mathbf{I}\right)^{-1} \mathbf{K}^T \mathbf{S}_y^{-1} \left(\mathbf{y} - \mathbf{F}(\mathbf{x}_i, \mathbf{b})\right). \qquad (1)$$

In Eq. 1, $\mathbf{x}$ is the state vector, i.e. the atmospheric quantities to be retrieved, $\mathbf{y}$ the vector of measurements (over a range of tangent heights), $\mathbf{S}_y$ the measurement error covariance matrix (assumed to be diagonal), λ the Levenberg-Marquardt weighting factor, $\mathbf{F}$ the radiative transfer (forward) model, $\mathbf{b}$ the forward model parameter vector, i the iteration number, and $\mathbf{K}$ is the Jacobian matrix ($\equiv \partial\mathbf{F}/\partial\mathbf{x}$).

The microwindow set and associated altitude ranges are listed in Table 1. The VMRs for molecules with absorption features in the microwindow set (see Table 2) were adjusted simultaneously with the COF_2 amount. All spectroscopic line parameters were taken from the HITRAN 2004 database (Rothman et al., 2005). The v3.0 COF_2 retrieval extends from a lower altitude of 12 km up to 34 km at the poles and 45 km at the equator, with the upper limit varying with latitude (see Table 1). During the retrieval the state vector is sampled on an altitude grid coinciding with the tangent altitudes of the measurements. The retrieved VMRs are then interpolated onto a uniform 1 km grid. For ACE spectra recorded at tangent heights that fall within the selected retrieval altitude range, the initial VMRs (which do not vary with season or latitude) for the least-squares fit are taken from the set of VMR profiles established by the ATMOS mission (Irion et al., 2002). The COF_2 spectral signal in ACE spectra recorded above the upper altitude retrieval limit (see Table 1) is generally below the noise level, making it impossible to directly retrieve VMRs at these altitudes. However, the ATMOS profile indicates that the COF_2 VMRs do not effectively drop to zero until ~ 55 km. To compensate, the portion of the retrieved VMR profile above the highest analysed ACE measurement is calculated by scaling this ATMOS, or *a priori*, profile in that altitude region; this scaling factor is determined during the least-squares fitting.

An ACE-FTS transmittance spectrum in the region of one of the microwindows is plotted in the top panel of Figure 1. This measurement comes from occultation ss11613 (recorded on 9 October 2005 south of Mexico, over the Pacific Ocean) at a tangent height of 28.9 km. The second panel reveals the calculated contribution to the measurement of COF_2 based on its retrieved VMR (~ 3%); three spectral features are clearly due to absorption of COF_2. The third panel gives the observed – calculated residuals for the retrieval without the inclusion of COF_2 in the forward model; the shape of these residuals matches well with the calculated COF_2 contribution. The bottom panel contains the observed – calculated residuals, indicating the goodness of the fit.

2.2. MIPAS spectra

The MIPAS instrument, a Fourier transform spectrometer, measures the thermal limb emission of the Earth's atmosphere in the mid-infrared spectral region, 685–2410 cm^{-1}. Launched in March 2002, the first two years of spectra were recorded at an unapodised resolution of 0.025 cm^{-1} (MOPD = 20 cm). The nominal scan pattern consisted of 17 tangent points per scan (FR17, FR = full resolution) from 6-68 km altitude with a minimum vertical spacing of 3 km. A mechanical degradation of the interferometer's mirror drive led to a cessation in measurements, with a resumption in operations in January 2005 at a reduced resolution of 0.0625 cm^{-1} (MOPD = 8 cm). The new nominal scan pattern consisted of 27 tangent points per scan (OR27, OR = optimised resolution) over altitude ranges that varied with latitude, from 5-70 km at the poles to 12-77 km at the equator; this variation, which approximately follows the tropopause shape, minimises the number of spectra lost to cloud contamination. The vertical spacing of OR27 scans ranges from 1.5 km at lower altitudes and 4.5 at higher altitudes. Note that the reduction in scan time associated with the lower spectral resolution resulted in an increase in the number of tangent points (an additional ten) within the limb scan, thus improving the vertical resolution. MIPAS data are available until April 2012, when communication with the ENVISAT satellite failed.

Retrievals were performed using v1.3 of the Oxford L2 retrieval algorithm MORSE (MIPAS Orbital Retrieval using Sequential Estimation; http://www.atm.ox.ac.uk/MORSE/) with ESA v5 L1B radiance spectra. The equivalent to Eq. 1 in an optimal estimation approach is (e.g. Rodgers, 2000):

$$\mathbf{x}_{i+1} = \mathbf{x}_i + \left[(1+\lambda)\mathbf{S}_a^{-1} + \mathbf{K}_i^T\mathbf{S}_y^{-1}\mathbf{K}_i^T\right]^{-1}\left\{\mathbf{K}_i^T\mathbf{S}_y^{-1}\left[\mathbf{y} - \mathbf{F}(\mathbf{x}_i, \mathbf{b})\right] - \mathbf{S}_a^{-1}\left[\mathbf{x}_i - \mathbf{x}_a\right]\right\}, \qquad (2)$$

where the new terms $\mathbf{x}_a$ and $\mathbf{S}_a$ represent the *a priori* estimate of $\mathbf{x}$ and its error covariance, respectively. However, rather than applying the above equation to the full set of measurements $\mathbf{y}$, MORSE uses a sequential estimation approach (Rodgers, 2000) and applies Eq. 2 successively to spectral subsets defined by each microwindow at each tangent height, which varies from scan to scan. For this work, the *a priori* estimate is taken from IG2 COF_2 profiles (Remedios et al., 2007); after each step of the sequential estimation, $\mathbf{x}_a$ and $\mathbf{S}_a$ are updated according to the results of the preceding step. The spectral microwindows and associated altitude ranges are listed in Table 3; the retrieval extends from a lower altitude of

228   7.5 up to 54.0 km, with the retrieved COF_2 VMRs interpolated from the tangent altitude grid

229   onto the same 1 km grid used by ACE. For COF_2 retrievals, the MORSE state vector

230   consists of the profile of COF_2 plus, for each microwindow (see Table 4), a profile of

231   atmospheric continuum and a radiometric offset (intended to remove any spectrally smooth

232   background variations within each microwindow, e.g., due to aerosols or thin clouds as well

233   as any residual altitude-dependent radiometric offsets). The forward model uses pressure,

234   temperature and the abundances of major contaminating species (H_2O, O_3, HNO_3, CH_4, N_2O

235   and NO_2) retrieved earlier from the same spectra (using MORSE), and IG2 profiles for other

236   minor gases. Spectroscopic data were taken from the MIPAS PF3.2 database (Flaud et al.,

237   2006), with the COF_2 data in this compilation coming from the HITRAN 2004 database

238   (Rothman et al., 2005). As with all MORSE VMR retrievals, the initial diagonal elements of

239   $\mathbf{S}_a$ were set to $(100\%)^2$; since MORSE retrieves ln(VMR) rather than VMR, the $\mathbf{S}_a$ diagonal

240   elements are profile-independent. The off-diagonal elements of $\mathbf{S}_a$ are set assuming a

241   (strong) vertical correlation length of 50 km, which provides regularisation at the expense of

242   vertical resolution. Finally, cloud-contaminated spectra were removed using the cloud index

243   method (Spang et al., 2004) with a threshold value of 1.8.

244   Note that unlike the ACE-FTS retrievals, MORSE retrieves COF_2 at altitudes well

245   above the VMR maximum, even though the information at high altitude is almost entirely

246   from the *a priori* profiles. Thus, any special treatment to scale the *a priori* is not required,

247   although, through the vertical correlation, the effect is similar to that explicitly applied for

248   ACE. Additionally, unlike ACE, MORSE uses MIPAS spectra with the Norton Beer strong

249   apodisation applied, hence $\mathbf{S}_y$ is banded rather than diagonal.

250   Figure 2 provides a plot that illustrates the COF_2 spectral feature in one of the

251   MIPAS microwindows. The top panel shows an averaged MIPAS radiance spectrum (in

252   black) interpolated to 20 km altitude from equatorial measurements taken in March 2010 for

253   the $772 - 775$ cm^{-1} microwindow; in red is the averaged calculated spectrum based on the

254   averaged retrieved VMRs, but without the inclusion of COF_2 in the forward model. The

255   second panel reveals the averaged calculated COF_2 contribution to the spectrum. The third

256   panel gives the observed – calculated residuals for the retrieval (in black), again without the

257   calculated COF_2 contribution; the shape of these residuals matches well with the calculated

258   COF_2 contribution in the second panel. Overlaid in red are the overall observed – calculated

259   residuals, indicating the goodness of the retrieval.

260

261   **3. Retrieval errors**

3.1. Infrared spectroscopy of carbonyl fluoride

Both ACE-FTS and MIPAS retrievals make use of the COF_2 linelist first released as part of the HITRAN 2004 database (and remaining unchanged for the HITRAN 2008 release), with partition data taken from the TIPS subroutine included in the HITRAN compilation. The retrievals reported here make use of three band systems of COF_2; these bands largely correspond to the ν_1 (1943 cm^{-1}; CO stretch), ν_4 (1243 cm^{-1}; CF_2 antisymmetrical stretch), and ν_6 (774 cm^{-1}; out-of-plane deformation) fundamental modes. In particular, the ACE-FTS retrieval makes use of spectroscopic lines in the ν_1 and ν_4 bands, whereas MIPAS uses ν_4 and ν_6.

Retrieving COF_2 VMR profiles from ACE-FTS and MIPAS spectra crucially requires accurate laboratory COF_2 spectroscopic measurements. Uncertainty in the laboratory data can directly contribute to systematic errors in the COF_2 retrievals. HITRAN employs error codes in the form of wavenumber errors for the parameters ν (line wavenumber) and δ_{air} (air pressure-induced line shift) and percentage errors for S (line intensity), γ_{air} (air-broadened half-width), γ_{self} (self-broadened half-width), and n_{air} (temperature-dependence exponent for γ_{air}). Each error code corresponds to an uncertainty range, but with no information as to how the parameters are correlated. In HITRAN the parameter δ_{air} (air pressure-induced line shift) for COF_2 is assumed to have a value of 0 cm^{-1} atm^{-1}. The same values of γ_{air} (0.0845 cm^{-1} atm^{-1} at 296 K), γ_{self} (0.175 cm^{-1} atm^{-1} at 296 K), and n_{air} (0.94) are used for all COF_2 spectral lines in HITRAN; according to the error codes these values are averages/estimates. They are taken from the work of May (1992), who determined these average parameters for selected lines in the ν_4 and ν_6 bands from measurements made by a tunable diode-laser spectrometer. For the ν_1 band most of the spectral lines used in the retrievals have stated intensity uncertainties $\geq$ 20%, for the ν_4 band between 10% and 20%, and for the ν_6 band the errors are listed as unreported/unavailable. After performing the MIPAS retrievals, the latest HITRAN2012 update was released, which revises the ν_6 band and includes several weak hot bands. The listed intensity uncertainties for this band have been revised to between 10% and 20%; spectral simulations indicate only minor intensity differences in the ν_6 band Q branch between the two linelists.

As part of the present study, a comparison was made between an N_2-broadened (760 Torr) composite spectrum of COF_2 (determined from multiple pathlength–concentration burdens) at 278 K and 0.112 cm^{-1} resolution, taken from the Pacific Northwest National Laboratory (PNNL) IR database (Sharpe et al., 2004) with a synthetic spectrum calculated using HITRAN2004 COF_2 line parameters for the same experimental conditions; the

maximum systematic error of the PNNL intensities is 2.5 % (1σ). The comparison reveals that the integrated ν_1 and ν_4 band intensities in the PNNL spectrum are ~ 15% higher than HITRAN, whereas the integrated intensity of the very strong Q branch in the ν_6 band of the PNNL spectrum is ~ 20–25 % higher than HITRAN. Furthermore, the air-broadened half-width in HITRAN for this Q branch appears to be too large at 760 Torr. May (1992) states that the average pressure-broadening coefficients, which are included in HITRAN, could not reproduce the experimental pressure-broadened spectra satisfactorily over the full Q branch region. The author suggests this may be a result of the *J*(rotational quantum number)-dependence of the pressure-broadening coefficients or other effects such as line mixing (Hartmann et al., 2008).

When selecting appropriate ACE microwindows from the ν_1 and ν_4 bands, it was noticed that a number of COF_2 lines suffered from systematic bad residuals. Since the COF_2 lines occur in clusters, i.e. are not isolated, there is a strong suggestion that line mixing is playing a role; unfortunately there are no available spectroscopic line parameters that describe line mixing for COF_2. Although the ACE v3.0 retrieval only employs lines with the best residuals, there could still remain a small contribution to the error from the neglect of line mixing. Lines in the ν_6 Q branch (employed in the MIPAS retrievals) are very tightly packed, so if line mixing effects are important, errors arising from their neglect will likely be larger for MIPAS retrievals compared with ACE. Unfortunately it is an almost impossible task to quantify these errors without accurate quantitative measurements at low temperatures and pressures. For the purposes of this work it is estimated that retrieval errors arising from COF_2 spectroscopy are at most ~ 15 %, however since different bands are used in the respective retrievals, it is likely there will be a relative spectroscopic-induced bias between the two schemes.

3.2. ACE-FTS spectra

The ACE v2.2 COF_2 data product has previously been validated against measurements taken by the JPL MkIV interferometer, a balloon-borne solar occultation FTS (Velazco et al., 2011). Unlike the v3.0 product, the upper altitude limit for the v2.2 retrieval is fixed at 32 km, with the scaled ACE *a priori* profile used above 32 km. MkIV and ACE v2.2 profiles from 2004 and 2005 agree well within measurement error, with the relative difference in mean VMRs less than ~ 10 %. However, it must be recognised that both retrievals make use of the same COF_2 spectroscopic data, which has an estimated systematic error of at most ~ 15 % (see Section 3.1).

330   For a single ACE profile, the 1σ statistical fitting errors are typically $\sim 10 - 30$ %

331   over most of the altitude range. These errors are random in nature and are largely determined

332   by the measured signal-to-noise ratios of the ACE-FTS spectra, i.e. measurement noise. For

333   averaged profiles, the random errors are small (reduced by a factor of $1/\sqrt{N}$, where N is the

334   number of profiles averaged) and the systematic errors dominate.

335   Spectroscopic sources of systematic error predominantly arise from the COF_2

336   HITRAN linelist (~ 15 %; see Section 3.1), with minor contributions from interfering species

337   that absorb in the microwindow regions. Since the baselines of the ACE-FTS transmittance

338   spectra and the VMRs of the interferers (H_2O, CO_2, O_3, N_2O, CH_4, NO_2, NH_3, HNO_3, HOCl,

339   HCN, H_2O_2, CCl_4, $ClONO_2$, N_2O_5) are fitted simultaneously with the COF_2 VMR, it is not a

340   trivial exercise to determine how much they contribute to the overall systematic error of the

341   COF_2 retrieval. In this work, the view is taken that the lack of systematic features in the

342   spectral residuals indicates that these contributions are small, at most 1 %.

343   In addition to spectroscopic errors, uncertainties in temperature, pressure, tangent

344   altitude (i.e. pointing) and instrumental line shape (ILS) all contribute to systematic errors in

345   the retrieved COF_2 profiles. To estimate the overall systematic error, the retrieval was

346   performed for small subsets of occultations by perturbing each of these quantities (b_j) in turn

347   by its assumed 1σ uncertainty (Δb_j), while keeping the others unchanged. The fractional

348   retrieval error, μ_j, is defined as

349

$$\mu_j = \left| \frac{VMR(b_j + \Delta b_j) - VMR(b_j)}{VMR(b_j)} \right|. \tag{3}$$

350

351

352   Note that for the ACE-FTS retrievals, pressure, temperature and tangent height are

353   not strictly independent quantities; tangent heights are determined from hydrostatic

354   equilibrium, and so these quantities are strongly correlated. For the purposes of this work,

355   only two of these quantities are altered: temperature is adjusted by 2 K and tangent height by

356   150 m (Harrison and Bernath, 2013). Additionally, ILS uncertainty is induced by adjusting

357   the field of view by 5 % (Harrison and Bernath, 2013). A small subset of occultations was

358   selected for this analysis. The fractional value estimates of the systematic uncertainties, and

359   their symbols, are given in Table 6. Assuming these quantities are uncorrelated, the overall

360   systematic error in the COF_2 retrieval can be calculated as

361

$$\mu^2_{systematic} = \mu^2_{spec} + \mu^2_{int} + \mu^2_T + \mu^2_z + \mu^2_{ILS} \, . \tag{4}$$

The total systematic error contribution to the ACE-FTS COF_2 retrieval is estimated to be ~16 %.

As discussed in Section 3.1, the COF_2 absorption signal in ACE-FTS spectra decreases relative to the noise as the retrieval extends to higher altitude despite the *a priori* profile indicating that the COF_2 VMRs do not effectively drop to zero until ~ 55 km. For this reason an upper altitude limit (see Table 1) is set; the retrieval is pushed as high in altitude as possible. The portion of the retrieved VMR profile above the highest analysed ACE measurement (i.e. the spectrum at the highest tangent height, just below the upper altitude limit) is calculated by scaling the *a priori* profile.

In an ACE retrieval, the calculated spectrum is generated from the sum of contributions from the tangent layer up to 150 km. For the highest analysed measurement, the retrieved VMR in the tangent layer is generated from the piecewise quadratic interpolation scheme (Boone et al., 2005; 2013), while the VMR in every layer above that will come from scaling the *a priori* profile; the scaling factor largely comes from forcing the calculated spectrum to match as best as possible the measured spectrum for this one measurement. If the shape of the *a priori* profile above the highest analysed measurement is incorrect, the contribution to the calculated spectrum from that altitude region will be incorrect for the second highest measurement analysed; the VMRs between the tangent layers of the two highest analysed measurements are adjusted in the retrieval to compensate. Therefore, errors in the *a priori* VMR profile will introduce systematic errors into the highest altitudes of the retrieved profile.

For the ACE-FTS, the vertical resolution is defined by the sampling unless the separation between measurements is less than the extent of the field-of-view, in which case the vertical resolution is limited to ~ 3 km. Although there is some variation in vertical resolution with the beta angle of the measurement, it is often the case that the vertical resolution at high altitudes (above ~ 40 km) is limited by the sampling, while at low altitudes it is limited by the field of view.

3.3. MIPAS spectra

394   The precision, or random error, of the retrieved COF_2 VMRs is calculated via the

395   propagation of the instrument noise and the *a priori* error through the standard optimal

396   estimation retrieval (using the MORSE code). The total retrieval covariance matrix

397   (neglecting systematic errors) is given by (Rodgers, 2000),

398

399
$$\hat{\mathbf{S}} = \mathbf{S}_a - \mathbf{S}_a \mathbf{K}^T \left(\mathbf{K} \mathbf{S}_a \mathbf{K}^T + \mathbf{S}_y \right)^{-1} \mathbf{K} \mathbf{S}_a .$$
    (5)

400

401   Note that this expression effectively represents a combination of the noise-induced random

402   error and the assumed *a priori* error covariance (this *a priori* contribution to the retrieval

403   error is sometimes called 'smoothing error'), and that some caution is required if

404   interpolating error profiles to different grids (von Clarmann, 2014). Profile levels with

405   random errors larger than 70%, mostly at the top and bottom of the retrieval range, are

406   discarded from the dataset and not used in the analysis. Since the *a priori* profiles have an

407   assumed error of 100%, this ensures that the retrieved profile levels contain, at worst, ~ 50%

408   contribution from the *a priori*. For a single profile, the noise error is typically 5–15%

409   between 20–40 km, covering the peak of the COF_2 VMR profile; over this range the

410   contribution to the retrieved profiles principally comes from the measurements. Outside this

411   range, the errors increase rapidly as the COF_2 VMR decreases, and the contribution to the

412   retrieved profiles from the *a priori* increases.

413   The total error is computed by propagating a number of independent error sources

414   expressed as spectra through the linearised form of Eq. 2, including both spectral correlations

415   and correlations through the pressure-temperature retrieval. For a single profile, the primary

416   error sources are the measurement noise followed by assumed uncertainties in the O_3

417   (stratosphere) and N_2O (troposphere) concentrations, which typically contribute 15%

418   uncertainty in retrieved COF_2 values. Spectroscopic errors, including those of interfering

419   species, are treated simply as a single, correlated error source. For COF_2 it is assumed that

420   there is an uncertainty of 0.001 cm^{-1} in line position, 15% in line strength and 0.1 cm^{-1} in

421   half-width. Figure 3 shows the single-profile error budget for COF_2, with total errors

422   typically 20–30% between 20–40 km. Additionally, the conversion of MIPAS COF_2 profiles

423   to absolute altitude for comparison with ACE-FTS profiles relies on the MIPAS pointing

424   information, which may lead to a vertical offset of a few hundred metres relative to ACE.

425   The sensitivity of the MIPAS COF_2 retrieval to the true state can be measured using

426   the averaging kernel matrix (Rodgers, 2000), **A**,

13

427

$$\begin{aligned}\mathbf{A} &= \mathbf{S}_a \mathbf{K}^T \left(\mathbf{K}\mathbf{S}_a \mathbf{K}^T + \mathbf{S}_y \right)^{-1} \mathbf{K}, \\ &= \mathbf{I} - \hat{\mathbf{S}}\mathbf{S}_a^{-1}\end{aligned} \qquad (6)$$

429

430 where $\mathbf{I}$ is the identity matrix. In general, for a given profile, rows of $\mathbf{A}$ are peaked functions,

431 peaking at the appropriate altitude range for the observation; the width of each function is a

432 measure of the vertical resolution of each COF_2 observation.

433   For the purposes of discussing averaging kernels and vertical resolution of the

434 MIPAS COF_2 retrieval, Figure 4 contains examples of typical retrieved profiles (from 22

435 December 2011) in cloud-free scenes for north polar winter (NPW), northern mid-latitude

436 (MID), equator (EQU) and south polar summer (SPS) conditions. Averaging kernels (i.e.

437 rows of the averaging kernel matrix) for these four retrievals are presented in Figure 5. The

438 retrieval altitude of each averaging kernel is indicated by the arrow with matching colour.

439 The MIPAS COF_2 retrieval is particularly sensitive in southern polar summer with the

440 combination of high concentrations and high stratospheric temperatures. Figure 6 provides a

441 plot of vertical resolution as a function of altitude for the four retrievals. Vertical resolution

442 is computed as dz_i/A_{ii}, where dz_i is the measurement/retrieval grid spacing at profile level i,

443 and A_{ii} is the corresponding diagonal element of the averaging kernel matrix. Figure 6

444 indicates the vertical resolution of the MIPAS retrievals is ~4–6 km near the COF_2 profile

445 peak, dropping off outside this range.

446

447

448 **4. Global distribution and vertical profiles**

449   For a detailed comparison between ACE-FTS and MIPAS observations, it was

450 decided to focus on one year of measurements between September 2009 and August 2010.

451 Note that since the differences in vertical resolution between the datasets are not too large,

452 these are not explicitly accounted for in the comparisons. Figure 7 provides a comparison

453 between individual profiles for four near-coincident sets of measurements; these are the four

454 closest sets available over this time period. The locations and times of the eight observations

455 can be found in Table 6. The plots also include the *a priori* profiles, and calculated

456 SLIMCAT profiles for the location and time of each ACE-FTS observation; these

457 calculations will be discussed in Section 5. In Figure 7, the upper altitudes of the ACE-FTS

458 profiles without error bars correspond to the regions where the *a priori* profiles are scaled in

459 the retrieval (see Section 3.2). Although the pairs of measurements were taken at slightly

460 different locations and times of day, near-coincident profiles should agree within

461 measurement error, unless there is significant atmospheric variability. COF_2 profiles initially

462 show an increase in VMR with altitude, peaking in the stratosphere and then decreasing with

463 higher altitude; the peak location depends on the latitude and time of year. On the whole, the

464 MIPAS and ACE profiles in Figure 7 agree well within random error bars. The profile for

465 ACE occultation sr34898 (at high northern latitudes in northern winter) shows a dip near 30

466 km due to part of the profile sampling descended COF_2-poor upper stratospheric air within

467 the polar vortex. The near-coincident MIPAS profile does not show such a strong dip, likely

468 due to the poorer vertical resolution of the MIPAS retrieval.

469 For the preparation of monthly zonal means over the period September 2009 to

470 August 2010, both ACE and MIPAS datasets were filtered to remove those observations

471 deemed 'bad'. Due to the relatively poor global coverage of ACE observations over this time

472 period, filtering had to be performed carefully; in this case only significant outliers were

473 removed. The MIPAS dataset contains substantially more observations over the globe, and

474 as discussed earlier, profile levels with random errors larger than 70% of the retrieved VMRs

475 were discarded. For each month, a global spike test was applied to all the remaining data. At

476 each altitude the mean and standard deviation of the ensemble were calculated. Any MIPAS

477 profiles with one or more VMRs outside 5σ of the mean VMRs were discarded. This spike

478 test was repeated until all remaining MIPAS profiles were within this 5σ range.

479 MIPAS observations indicate a very minor diurnal variation in COF_2 VMRs, well

480 below the measurement error. Therefore, in this work ACE and MIPAS zonal means were

481 produced without any consideration of the local solar time of the individual measurements.

482 Figure 8 provides a direct side-by-side comparison of MIPAS and ACE zonal means for each

483 of the twelve months, revealing the seasonal variation in the COF_2 distribution. The plotted

484 VMRs are the averages for each month of all filtered data at each altitude within 5˚ latitude

485 bins. The highest COF_2 VMRs appear at ~ 35 km altitude over the tropics, which receive the

486 highest insolation due to the small solar zenith angle; these peaks are located ~ 10ºS for

487 December to April, and ~ 10ºN for June to October. COF_2 has a lifetime of ~3.8 years

488 (calculated from SLIMCAT; refer to Section 5) and is transported polewards by the Brewer-

489 Dobson circulation. As can be seen in the figure, the plots are not symmetric about the

490 equator. For example, an additional peak at southern high latitudes is most prominent in

491 January/February 2010; this will be further discussed in Section 5. The observations in

492   Figure 8 also demonstrate the presence of a strong southern hemisphere (SH) polar vortex in
493   September 2009 and August 2010; the associated low COF_2 VMRs at high southern latitudes
494   are a consequence of the descent of air in the vortex from the upper stratosphere / lower
495   mesosphere where COF_2 VMRs are low. The break-up of the SH polar vortex occurs around
496   November 2009 and begins to form again around June 2010. The northern hemisphere (NH)
497   polar vortex is intrinsically weaker and varies considerably from year to year. For the year
498   analysed here the vortex appeared strongest in December 2009 and January 2010.   The
499   overall atmospheric distribution of COF_2 is determined by a complicated combination of its
500   production, lifetime, and transport.   More details on these atmospheric processes will be
501   discussed in Section 5, along with a discussion of the SLIMCAT CTM.

502   Since there are only a maximum of 30 ACE-FTS profiles measured per day,
503   compared to ~1300 for MIPAS (OR27), the global coverage of the ACE observations
504   between September 2009 and August 2010 is poorer and noisier in appearance. Despite this,
505   the ACE observations agree well with MIPAS, apart from the apparent high bias in the
506   MIPAS VMRs, which will be discussed later in this section. As examples, note the good
507   agreement at mid- to high-latitudes in the SH between regions with high VMRs in December
508   2009 and March 2010, and low VMRs in August 2010; in the tropical regions, high VMRs
509   peaking north of the equator in October 2009 and August 2010, and south of the equator in
510   February 2010; at mid- to high-latitudes in the NH between regions with high VMRs in
511   September 2009, and low VMRs in February and March 2010.

512   Since zonal mean plots do not provide an indication of measurement errors, a
513   representative set of individual latitude bins are plotted in Figure 9 with error bars; all errors
514   are defined as the standard errors of the bin means. Such plots are useful to inspect biases
515   between datasets. Note that SLIMCAT calculations are also included in this figure; these
516   will be further discussed in Section 5. ACE random errors are largest close to the tropics at
517   the highest altitudes of the retrieval (where the black error bars are longest, ~ 35–45 km). At
518   these altitudes COF_2 features in ACE-FTS spectra are weaker, so the relative noise
519   contribution to the retrieved VMRs is larger. The retrieved ACE VMR profiles in this region
520   have a rather flat appearance, whereas the corresponding MIPAS profiles are peaked. The
521   MIPAS VMRs themselves are biased as much as 30% higher than ACE, although there is
522   overlap between the error bars. This MIPAS–ACE bias is believed to arise predominantly
523   from the large COF_2 spectroscopic errors, which make differing contributions to the ACE
524   and MIPAS profiles due to the different microwindows used in the respective retrieval
525   schemes. At the very highest altitudes (above ~ 50 km), the ACE VMRs drop to zero, and

526 the MIPAS VMRs approach ~ 50 ppt; these differences result from the different *a priori*
527 profiles used for the two retrieval schemes. A more detailed discussion on this point will be
528 made in Section 5. For the August 2010 25–30ºS plot in Figure 9, the increase at the top of
529 the retrieved altitude range (above ~ 40 km) likely results from the approach used to scale the
530 *a priori* above the highest analysed measurement (refer to Section 3.2). Figure 9 also reveals
531 a bias at high latitudes in the summer, where the ACE and MIPAS profiles peak just above
532 30 km. (The summer SH high-latitude peak corresponds to a secondary maximum in the
533 VMR distribution; the origin of this will be discussed in Section 5.) As in the tropics,
534 MIPAS VMRs at the peak are ~ 30% higher than ACE. Note that for these particular
535 months, the ACE-FTS was taking many measurements at high latitudes, hence the smaller
536 error bars.

537

538 **5. Comparison with SLIMCAT 3D Chemical Transport Model**

539 ACE and MIPAS observations have been compared with output from the SLIMCAT
540 off-line 3D CTM. SLIMCAT calculates the abundances of a number of stratospheric gases
541 from prescribed source-gas surface boundary conditions and a detailed treatment of
542 stratospheric chemistry, including the major species in the O_x, NO_y, HO_x, Cl_y and Br_y
543 chemical families (e.g. Chipperfield, 1999; Feng et al., 2007). The model uses winds from
544 meteorological analyses to specify horizontal transport while vertical motion in the
545 stratosphere is calculated from diagnosed heating rates. This approach gives a realistic
546 stratospheric circulation (Chipperfield, 2006; Monge-Sanz et al., 2007). The troposphere is
547 assumed to be well-mixed.

548 For this study SLIMCAT was integrated from 2000 to 2012 at a horizontal
549 resolution of 5.6^o x 5.6^o and 32 levels from the surface to 60 km; the levels are not evenly
550 spaced in altitude, but the resolution in the stratosphere is ~ 1.5–2.0 km. The model uses a σ-
551 θ vertical coordinate (Chipperfield, 2006) and was forced by European Centre for Medium
552 Range Weather Forecasts (ECMWF) reanalyses (ERA-Interim from 1989 onwards). The
553 volume mixing ratios of source gases at the surface level were specified using data files
554 compiled for the 2010 WMO ozone assessment (WMO/UNEP, 2011). These global mean
555 surface values define the long-term tropospheric source gas trends in the model.

556 A previous run of SLIMCAT, used in an investigation of the atmospheric trends of
557 halogen-containing species measured by the ACE-FTS (Brown, et al., 2011), neglected the
558 COF_2 contribution from the atmospheric degradation of HFCs. This has now been remedied
559 for the most important HFCs. In total, this run of SLIMCAT calculates COF_2 contributions

560   arising from the degradation of CFC-12, CFC-113, CFC-114, CFC-115, HCFC-22, HCFC-

561   142b, HFC-23, HFC-134a, HFC-152a, Halon 1211, and Halon 1301. A number of these

562   molecules, e.g. HFC-23, are included even though they make no appreciable contribution to

563   the formation of COF_2 compared with the major source gases. Some other HFCs, e.g. HFC-

564   125, which similarly make minimal contribution, are not included in the model. In addition

565   to providing a direct comparison with satellite observations, the new SLIMCAT calculations

566   have been used to show where COF_2 is produced and which source gases have produced it.

567   Most COF_2 is produced in the tropics where solar insolation is highest. Figure 10 provides

568   plots of the loss rates (annual mean zonal mean; pptv/day) for the three main source gases

569   which produce COF_2. As can be seen, the largest contributing COF_2 source at ~30–35 km is

570   CFC-12, followed by CFC-113 (approximately a factor of 10 smaller). HCFC-22 is the

571   second largest contributing source gas overall, however its contribution peaks low in the

572   troposphere (not relevant for stratospheric COF_2) and higher up in the stratosphere (~40–45

573   km). CFC-12 and CFC-113 are removed mainly by photolysis ~20–40 km; above this

574   altitude range the abundances of CFC-12 and CFC-113 tend to zero so that they make only a

575   small contribution to the formation of COF_2. On the other hand, HCFC-22 is mainly

576   removed from the atmosphere by reaction with OH. Since this reaction is slower, HCFC-22

577   persists higher into the stratosphere than CFC-12 and CFC-113 and can therefore lead to

578   COF_2 production in the upper stratosphere and lower mesosphere. Individual contributions

579   from molecules other than these three are typically a small fraction of 1%. In the altitude

580   region below the maximum COF_2 VMRs at all locations there is net production of COF_2,

581   while at higher altitudes there is net loss. The primary loss of COF_2 in the atmosphere occurs

582   via photolysis, with an additional secondary loss mechanism through reaction with $O(^1D)$;

583   SLIMCAT calculates the relative contributions as 90 % and 10 %, respectively. Figure 10

584   also contains a plot of the COF_2 annual mean zonal total loss rate.

585   SLIMCAT has also been used to estimate the atmospheric lifetime of COF_2 by

586   simply dividing the total modelled atmospheric burden by the total calculated atmospheric

587   loss rate. The total calculated mean atmospheric lifetime is ~3.8 years. This lifetime varies

588   slightly between the hemispheres, 3.76 years in the south and 3.82 years in the north. In the

589   lower stratosphere COF_2 can be regarded as a long-lived tracer (local lifetime of many years).

590   Therefore, its tracer isopleths follow the typical tropopause-following contours of any long-

591   lived tracer. In this sense, COF_2 is analogous to NO_y which is produced from N_2O. It has

592   been checked as part of this work that a correlation plot of COF_2 with its major source, CFC-

593 12, is compact in the lower stratosphere, at altitudes below the region of COF_2 maxima

594 (Plumb and Ko, 1992).

595 As discussed in Section 4, Figure 7 contains a comparison between individual ACE-

596 FTS and MIPAS profiles for the measurements specified in Table 6. This figure also

597 contains SLIMCAT profiles calculated for the location and time of each ACE-FTS

598 observation. In comparison with the retrieved portion of the ACE profiles (marked by black

599 error bars), the calculated SLIMCAT VMRs are generally slightly lower; the agreement with

600 MIPAS is worse, however it must be acknowledged that the two sets of measurements are

601 not strictly coincident. Additionally, SLIMCAT captures the VMR 'dip' observed for ACE

602 occultation sr34898 (at 67.27ºN on the vortex edge, 4 February 2010) near 30 km altitude,

603 confirming that this profile samples air from the polar vortex. This explanation is supported

604 by the corresponding ACE HF profile, which shows an enhancement near 30 km due to the

605 sampling of descended HF-rich upper-stratospheric air from the polar vortex.

606 Figure 11 provides a comparison between SLIMCAT and ACE zonal means. In

607 order to increase the latitude coverage for the comparison and reduce the noise over some of

608 the latitude bands, the plotted ACE data are averages of the data in Figure 8 (September 2009

609 to August 2010) with data from the previous year; on the scale of the Figure there is no

610 significant variation in the seasonal pattern as measured by the ACE-FTS. Figure 11 reveals

611 that the model agrees well with the ACE observations and reproduces very well the

612 significant seasonal variation, although SLIMCAT produces slightly lower VMRs and the

613 ACE measurements still suffer from measurement noise. Comparing the SLIMCAT zonal

614 means (in Figure 11) with those for MIPAS (in Figure 8) again demonstrates the good

615 agreement in seasonal variation, but the MIPAS VMRs have a noticeably high bias compared

616 with the model.

617 Figure 9 shows a representative set of SLIMCAT profiles in 5º latitude bins from the

618 September 2009 to August 2010 time period, along with averaged ACE and MIPAS profiles.

619 These demonstrate a very good agreement between the SLIMCAT calculations and ACE

620 observations, although above ~ 35 km this agreement is somewhat worse, particularly the

621 upper parts of the ACE profiles (without error bars) which are derived from the scaled *a*

622 *priori* profile and susceptible to systematic errors (see Section 3.2). Whereas the ACE

623 VMRs drop to zero at ~ 55 km, the SLIMCAT VMRs do not reach zero even near the model

624 top level around 60 km due to the calculated ongoing production of COF_2 from HCFC-22

625 (see Figure 10). MIPAS VMRs similarly do not drop to zero, principally because the *a priori*

626 profiles make a larger contribution to the retrieved VMRs at these altitudes. Unfortunately,

627   neither ACE nor MIPAS measurements are able to validate the SLIMCAT model HCFC-22 /

628   COF_2 VMRs near 55 – 60 km.

629   In autumn when solar heating of the relevant polar region comes to an end, a

630   stratospheric polar vortex begins to form. This is a large-scale region of air contained within

631   a strong westerly jet stream that encircles the polar region. Reaching maximum strength in

632   the middle of winter, the polar vortex decays as sunlight returns to the polar region in the

633   spring. Polar vortices, which extend from the tropopause up into the mesosphere, are quasi-

634   containment vessels for air at cold temperatures and low-ozone content. They play a critical

635   role in polar ozone depletion, more so in the Antarctic, where the vortex is larger, stronger,

636   and longer-lived than in the Arctic. The SLIMCAT September 2009 (09/2009) plot in Figure

637   11 demonstrates the presence of a strong SH polar vortex by the low COF_2 VMRs at high

638   southern latitudes; as mentioned earlier this is a consequence of the descent of upper-

639   stratospheric air where COF_2 VMRs are very low. The breakup of the SH polar vortex as

640   simulated by SLIMCAT occurs around November 2009 (11/2009) and begins to form again

641   around June 2010 (06/2010). On the other hand, the descent of upper stratospheric air

642   corresponding to the onset of the NH polar vortex is less obvious due to the intrinsically

643   lower COF_2 VMRs in the NH summer; SLIMCAT observations suggest the northern polar

644   vortex is present from December 2009 to January 2010.

645   Although some of the COF_2 present at mid- and high-latitudes can be attributed to

646   transport of COF_2-rich tropical air via the Brewer–Dobson circulation (a slow upwelling of

647   stratospheric air in the tropics, followed by poleward drift through the mid-latitudes, and

648   descent in the mid- and high-latitudes), this cannot account for the secondary maximum in

649   VMR (~ 31 km) present in the SH polar region for which an atmospheric chemistry

650   explanation is needed. Diagnosis of the model rates shows that in summer, photochemical

651   production of COF_2 extends to the pole in the middle stratosphere (i.e. in polar day). Further

652   diagnosis of the first-order loss rates of the main COF_2 precursors shows that photolysis and

653   reactions with $O(^1D)$ are symmetrical between the hemispheres. The only precursor loss

654   reaction which shows significant hemispheric asymmetry is the temperature-dependent

655   reaction of CHF_2Cl (HCFC-22) + OH. As the SH polar summer mid-stratosphere is around

656   10 K warmer than the corresponding location in the NH, this reaction provides a stronger

657   source of COF_2 in SH summer compared to the Arctic and contributes to this secondary

658   maximum. Indeed, in a model sensitivity run where the production of COF_2 from HCFC-22

659   was switched off, this secondary SH summer peak disappeared. While the first-order loss

660   rates of the COF_2 source gas precursors are generally symmetrical between the hemispheres,

661   this is not true for the source gases themselves. Differences in the meridional Brewer-

662   Dobson circulation, with stronger mixing to the pole in the north and stronger descent in the

663   south, lead to differences in the distribution of COF_2 precursors. This leads to differences in

664   COF_2 production resulting in the observed and modelled hemispheric asymmetry in COF_2 at

665   middle latitudes.

666

667   **6. Trends**

668   As mentioned in the introduction, there is evidence that the atmospheric abundance

669   of COF_2 is increasing with time (Duchatelet et al., 2009; Brown et al., 2011). Although the

670   atmospheric abundances of COF_2 source gases such as CFC-12 and CFC-113 are currently

671   decreasing, HCFC-22 and the minor HFC contributors are still on the increase. Figure 1–1 of

672   the 2010 WMO ozone assessment (WMO/UNEP, 2011) shows the trends in mean global

673   surface mixing ratios for these two species during the 1990–2009 time period. The CFC-12

674   growth rate is observed to reduce slowly from 1990, plateauing around 2003–2004, after

675   which it becomes negative, i.e. an overall loss of CFC-12. In comparison, the growth rate of

676   HCFC-22 has been relatively constant since 1990, with a slight increase in growth rate

677   occurring around 2007.

678   A number of previous studies have quantified the trend in atmospheric COF_2 over

679   time. For the Jungfraujoch 1985 to 1995 time series (46.5ºN latitude, 8.0ºE longitude), a

680   period when CFC-12 was still increasing the atmosphere, an average COF_2 linear trend of 4.0

681   ± 0.5%/year was derived (Mélen et al., 1998). COF_2 trends from more recent studies are

682   considerably lower, largely due to the phase out of its principal source gas, CFC-12. A trend

683   of 0.8 ± 0.4 %/year has recently been derived from ACE data for 2004 to 2010 (Brown et al.,

684   2011). Since the majority of halogenated source gases reach the stratosphere by upwelling

685   through the tropical tropopause region, the ACE COF_2 trend was determined by averaging

686   measurements in the latitude band 30ºS to 30ºN between 30 and 40 km altitude; effectively

687   the seasonal variation in COF_2 was averaged out. For the Jungfraujoch 2000 to 2007 time

688   series, a linear trend of 0.4 ± 0.2%/year was derived (Duchatelet et al., 2009). The observed

689   COF_2 seasonal variation, which was removed using a cosine function, had maxima towards

690   the end of February (winter) and minima in late summer when photodissociation processes

691   are at their maximum. In contrast, trends calculated from older SLIMCAT runs for Brown et

692   al. (2011) and Duchatelet et al. (2009) are –1.3 ± 0.4%/year and –0.5 ± 0.2%/year,

693   respectively. For the latter of these, it was noted that the SLIMCAT time series suffered

694   from several discontinuities in the operational ECMWF meteorological data, for which the

695 vertical resolution had been changed several times; this resulted in a decrease in the

696 SLIMCAT COF_2 columns between 2002 and 2006. For the present work, this is no longer a

697 problem because ERA-Interim reanalyses, which use a consistent version of the ECMWF

698 model, are now used by SLIMCAT (e.g. Dhomse et al., 2011).

699   In this section, ACE and MIPAS time series are derived as a function of altitude and

700 latitude. As discussed previously, e.g. in Harrison and Bernath (2013), ACE latitude

701 coverage is uneven. For data between January 2004 and September 2010 (the last month for

702 which ACE v3.0 data is usable due to problems with the pressure / temperature *a priori*), the

703 18 10º latitude bins used for the ACE time series contain, from southernmost to

704 northernmost, 1000, 1323, 5265, 1776, 796, 608, 482, 420, 390, 394, 339, 413, 650, 1062,

705 2012, 4828, 1875, 1315 occultations, respectively, i.e. over three-quarters of the

706 measurements lie in latitude bins poleward of 50° S/N. On the other hand, MIPAS data

707 coverage over the globe is more even and extensive, apart from some periods during 2004 –

708 2006 when nominal mode measurements were not made.

709   Figure 12 illustrates the MIPAS and SLIMCAT time series for COF_2 between July

710 2002 and April 2012 for all latitudes at selected altitudes; both datasets were binned in 10º

711 latitude bands. (Due to the sparse nature of the ACE-FTS measurements, such a plot has not

712 been provided for the ACE dataset.) An annual cycle is readily observed, and as expected its

713 phase is opposite in each hemisphere. The amplitude of this cycle is largest near the poles;

714 note that the maxima in the plot at 20.5 km altitude correspond to the descent of COF_2 in

715 winter polar vortices. Close inspection of Figure 12, particularly the plots above 30 km, also

716 reveals the presence of the quasi-biennial oscillation (QBO) signal, which is strongest in the

717 tropics. Overall, there is good agreement between the MIPAS and SLIMCAT plots in terms

718 of the overall latitude-altitude pattern, however, as noted before, the MIPAS VMRs are

719 biased high; for example, maxima over the tropics as much as ~ 25% and maxima near the

720 poles as much as ~ 50%.

721   Figure 13 provides the time series for five altitude – latitude bin combinations of

722 ACE, MIPAS and SLIMCAT data; for ease of viewing, this plot does not include errors. In

723 all plots, the main features in the time series agree well. Note the observed QBO signal for

724 all three datasets, which is stronger in the two tropical plots and weaker in the high-northern-

725 latitude plot. In the top two plots of Figure 13 MIPAS is biased high, although less so at 20.5

726 km. As established previously (refer to Figure 9), this is a feature of the MIPAS dataset at

727 the high southern latitudes. The agreement between ACE and SLIMCAT is somewhat better,

728 agreeing within the errors of the ACE data, although less so at high southern latitudes.

729   COF$_2$ trends at each altitude for all 18 latitude bins have been calculated from

730   monthly percentage anomalies in COF$_2$ zonal means, $C^{z,\theta}(n)$, defined as

731
$$C^{z,\theta}(n) = 100 \frac{VMR^{z,\theta}(n) - \sum_{m=1}^{12} \delta_{nm} \overline{VMR}^{z,\theta}(m)}{\sum_{m=1}^{12} \delta_{nm} \overline{VMR}^{z,\theta}(m)} ,\qquad (7)$$

732   where n is a running index from month zero to 80 (January 2004 to September 2010),

733    $VMR^{z,\theta}(n)$ is the corresponding mixing ratio at altitude z and latitude θ, $\overline{VMR}^{z,\theta}(m)$ is the

734   average of all zonal means for each of the twelve months, m, and δ_{nm}, although not used in its

735   strict mathematical sense, is one when index n corresponds to one of the months m and is

736   zero otherwise. In order to compare the three datasets, the same time period was used for

737   each analysis. Such an approach essentially removes the annual cycle and the effect of biases

738   in VMRs; the trend is simply equated to the 'slope' of the linear regression between $C^{z,\theta}(n)$

739   and the dependent variable $n/12$. The inclusion of additional terms such as the annual cycle

740   and its harmonics resulted in no additional improvement in the regression.

741   Figure 14 presents the annual percentage trends (January 2004 to September 2010)

742   for ACE, MIPAS, and SLIMCAT as a function of latitude and altitude. The plotting range

743   has been chosen to cover the maximum VMR features in the COF$_2$ global distributions; this

744   broadly follows the upper altitude range of the actual ACE retrievals and removes portions of

745   the MIPAS profiles that have the largest contributions from the *a priori* profile. Note that

746   whereas the MIPAS time series used to derive trends contains data for 67 distinct months in

747   all latitudes band, the number of months of ACE data available varies from as low as 15 to as

748   high as 63 in each latitude band. Errors were not explicitly treated in the linear regression of

749   the SLIMCAT outputs, but were for the MIPAS and ACE VMRs. Note that as the MIPAS

750   and ACE trends approach zero, the ratio to their 1σ uncertainties drops well below one.

751   Broadly speaking, the trends for any ACE/MIPAS latitude-altitude region in Figure 14 which

752   appear predominantly blue or green become more statistically significant when the individual

753   contributions are averaged.

754   The MIPAS plot in Figure 14 indicates that between 2004 and 2010, COF$_2$ has

755   increased most rapidly (approaching ~ 4% per year) at altitudes above ~25 km in the

756   southern latitudes and at altitudes below ~25 km in the northern latitudes. The ACE plot

757   broadly agrees with respect to these two regions of largest positive trend, although their

758   magnitudes are slightly lower. Additionally, the ACE trends in the tropical region are

759   predominantly negative, which somewhat agrees with SLIMCAT below 25 km.

23

The SLIMCAT plot contains a number of features which agree with both the MIPAS and ACE plots. In particular, the SLIMCAT plot indicates a decrease in COF_2 in the tropical region (between 20˚S and 10˚N), although the largest decrease occurs at ~27 km and 0˚ latitude; ACE agrees better than MIPAS in this region, except for a narrow altitude range ~ 30 km where the ACE trends are slightly positive. Outside the tropics, the SLIMCAT plot agrees better with MIPAS, in particular for the regions of largest positive trends which occur at high southern latitudes above 30 km and northern latitudes below ~ 25 km.

An additional SLIMCAT run has been performed with dynamics arbitrarily fixed to those for the year 2000; results from this run give a 'clean' COF_2 signal without the complication of changes in stratospheric dynamics. Trends have been calculated in the same manner as above, and plotted in the lowest panel of Figure 14. Compared with trends for the 'control' SLIMCAT run, those for the fixed-dynamics run lie predominantly between 0 and 1 %, with a relatively uniform distribution throughout the stratosphere. This indicates that the variations in SLIMCAT trends, and by extension the regions of agreement with MIPAS and ACE, result from changes in stratospheric dynamics between January 2004 and September 2010.

One might expect that the decreasing SLIMCAT trends over the 2004 – 2010 period in the lower tropical stratosphere, where the air is youngest, result directly from the decrease in mean global surface mixing ratio of CFC-12 since ~2003–2004 (WMO/UNEP, 2011); note that HCFC-22 produces COF_2 at higher altitudes. However, the absence of any negative tropical trends in the fixed-dynamics SLIMCAT plot indicates that this feature must result from dynamical considerations.

The analyses used to force the SLIMCAT calculations provide information on the stratospheric circulation, but do not allow for any rigorous explanation of the changing stratospheric dynamics that are responsible for the observed trends. Interestingly, the two regions of large positive trends in the ACE, MIPAS, and SLIMCAT plots correspond quite well to the regions of positive age of air trends, as reported by Stiller et al. (2012); see their Figure 10. Additionally, the region of positive trends in the tropics ~28-35 km, contained in the ACE plot, more-or-less agrees with the corresponding feature in the age-of-air-trend plot. As discussed by Stiller et al. (2012), it is likely that variations in atmospheric mixing have occurred over the observation period. The regions of maximum COF_2 trends must result from increased in-mixing of COF_2-rich air, possibly due to major sudden stratospheric mid-winter warmings. The negative trends in the tropics could result from an increase in the rate of upwelling over the observation period. MIPAS observations of CFC-11 and CFC-12,

794 reported by Kellmann et al. (2012), reveal similar variations in trends over the globe. For
795 example, despite these molecules slowly being removed from the atmosphere, a positive
796 trend is readily observed in the stratosphere between ~10–90ºS and ~ 22–30 km altitude.

797   Overall global trends in COF_2 VMRs, weighted by the average VMRs at each
798 altitude and latitude, have been calculated from the three datasets using errors in trends as
799 determined from the linear regression; 0.30 ± 0.44 %/year for ACE, 0.85 ± 0.34 %/year for
800 MIPAS, and 0.88 %/year for SLIMCAT. Note that these values only apply to the January
801 2004 to September 2010 time period. Any spectroscopic deficiencies that might lead to
802 regional biases in the ACE and MIPAS datasets should have been removed by taking
803 percentage anomalies, however there still remains the possibility of systematic errors that
804 contribute to time-dependent biases. The pressure-temperature retrievals for ACE v3.0
805 processing assume a rate of increase of 1.5 ppm/year for the CO_2 VMRs, which are assumed
806 to have a single profile shape for all locations and seasons. This rate of increase is lower than
807 the accepted value of $1.90 – 1.95$ ppm/year (0.5%/year) as used, for example, in IG2 CO_2
808 profiles for MIPAS retrievals. By the end of the time series, ACE v3.0 CO_2 VMRs are too
809 low by ~0.7 %. This translates into a small time-dependent negative bias in COF_2 VMR,
810 meaning that the trend derived from ACE v3.0 data is biased low by on average ~0.1 %/year,
811 although it is not obvious how the bias varies with latitude and altitude.

812   Plans are currently underway to create a new ACE processing version 4.0, in which
813 it is assumed that the CO_2 VMR increases by 0.5%/year and in which age of air
814 considerations are used to generate the vertical CO_2 VMR profile as a function of latitude and
815 time of year (Toon, 2012). It is anticipated that the new v4.0 will enable more accurate
816 trends to be derived. The ACE-FTS continues to take atmospheric measurements from orbit,
817 with only minor loss in performance; it will be possible to extend the COF_2 time series to the
818 present day and beyond.

819

820

821 **7. Conclusions**

822   Carbonyl fluoride (COF_2) is the second most abundant 'inorganic' fluorine reservoir
823 in the stratosphere with main sources being the atmospheric degradation of CFC-12 (CCl_2F_2),
824 HCFC-22 (CHF_2Cl), and CFC-113 ($CF_2ClCFCl_2$), species whose emissions are
825 predominantly anthropogenic.

826   This work reports the first global distributions of carbonyl fluoride in the Earth's
827 atmosphere using infrared satellite remote-sensing measurements by the ACE-FTS, which

828   has been recording atmospheric spectra since 2004, and the MIPAS instrument, which has

829   recorded thermal emission atmospheric spectra between 2002 and 2012. The observations

830   reveal a high degree of seasonal and latitudinal variability over the course of a year, and

831   agree well with the output of the SLIMCAT model, although MIPAS VMRs are biased high

832   relative to ACE by as much as ~ 30 %. This MIPAS–ACE bias is believed to arise

833   predominantly from the large COF_2 spectroscopic errors, which make differing contributions

834   to the ACE and MIPAS profiles due to the different microwindows used in the two retrieval

835   schemes.

836   The maximum in the COF_2 VMR distribution occurs at ~30–35 km altitude in the

837   tropics where solar insolation is highest; this region is dominated by COF_2 formed from the

838   photolysis of CFC-12 and CFC-113. The first-order loss rates of the main COF_2 precursors

839   are symmetrical between the hemispheres, except for the HCFC-22 + OH reaction, which is

840   temperature dependent; a secondary maximum at ~25–30 km altitude is present at high

841   latitudes in SH summer due to the mid-stratosphere being around 10 K warmer than the

842   corresponding location in the NH summer. There is also asymmetry in the distribution of

843   COF_2 precursors due to differences in the meridional Brewer-Dobson circulation, with

844   stronger mixing to the pole in the north and stronger descent in the south; this results in larger

845   VMRs at mid- and high-latitudes in the SH.

846   Between January 2004 and September 2010 COF_2 grew most rapidly at altitudes

847   above ~25 km in the southern latitudes and at altitudes below ~25 km in the northern

848   latitudes, whereas it declined most rapidly in the tropics. These variations are attributed to

849   changes in stratospheric dynamics over the observation period. The overall COF_2 global

850   trend over this period is calculated as 0.85 ± 0.34 %/year (MIPAS), 0.30 ± 0.44 %/year

851   (ACE), and 0.88 %/year (SLIMCAT).

852

853   **Author contribution**

854   Based on an idea from PFB, JJH devised the study and performed the data analysis.

855   AD performed the MIPAS retrievals and SC filtered and prepared the data for analysis. CDB

856   performed the ACE-FTS retrievals and JJH filtered and prepared the data for analysis. PFB

857   allowed the use of ACE data in this work. MPC and SD ran the SLIMCAT model and

858   provided additional explanation of the outputs. JJH prepared the manuscript with

859   contributions from MPC and AD.

860

861   **Acknowledgements**

Figure Captions

Figure 1. Top panel: an ACE-FTS transmittance spectrum covering the 1929.9–131.3 cm^{-1} microwindow for occultation ss11613 (recorded on 9 October 2005 south of Mexico, over the Pacific Ocean) at a tangent height of 28.9 km. Second panel: the calculated COF_2 transmittance contribution to the measurement (~ 3%). Third panel: the observed – calculated residuals for the retrieval without the inclusion of COF_2 in the forward model. Bottom panel: the total observed – calculated residuals for the retrieval.

Figure 2. Top panel: an averaged MIPAS radiance spectrum (in black) for equatorial measurements (3547) taken in March 2010 covering the $772 - 775$ cm^{-1} microwindow and interpolated to 20 km altitude; in red is the averaged calculated spectrum without the inclusion of COF_2 in the forward model. Second panel: the calculated COF_2 contribution to the spectrum. Bottom panel: the observed – calculated residuals for the retrieval, with and without COF_2 included in the forward model (in red and black, respectively).

Figure 3. The single-profile total error budget for the MIPAS COF_2 retrieval (mid-latitude day-time conditions). The total error is computed by propagating a number of independent error sources expressed as spectra through the linearised form of Eq. 2, including both spectral correlations and correlations through the pressure-temperature (PT) retrieval. Note that NESR is the noise equivalent spectral radiance, SHIFT refers to the uncertainty in the spectral calibration (± 0.001cm^{-1}), SPECDB refers to spectroscopic database errors, which are treated simply as a single, correlated error source, and GRA refers to the uncertainty due to an assumed $\pm$ 1K / 100 km horizontal temperature gradient. More details are contained in the text. Total errors are typically 20–30% between 20–40 km.

Figure 4. Examples of typical MIPAS retrievals of COF_2 profiles in cloud-free scenes for north polar winter (NPW), northern mid-latitude (MID), equator (EQU) and south polar

896   summer (SPS) conditions.   Retrieved profiles are shown by circles with error bars
897   representing the retrieval random error, open symbols are profile levels where this exceeds
898   70 % of the VMR and so excluded from these analyses.   The lines represent the *a priori*
899   profiles for each retrieval (the *a priori* error is assumed to be 100 %, i.e. a factor of two
900   uncertainty). Profiles are all selected from 22 December 2011, details as follows: NPW Orbit
901   51319, (80.0ºN, 98.8ºW); MID Orbit 51312, (37.6ºN, 10.4ºE); EQU Orbit 51312, (0.3ºS,
902   96.4ºW); SPS Orbit 51312, (81.6ºS, 44.9ºE).

903

904   **Figure 5**.   Averaging kernels (i.e., rows of the averaging kernel matrix) of the retrievals
905   shown in Figure 4. The retrieval altitude of each averaging kernel is indicated by the arrow
906   with matching colour. The solid black line represents the summation of all the elements of
907   each averaging kernel.   The figures in each panel refer to 'degrees of freedom for signal'
908   (DFS), i.e., the number of independent pieces of information in each profile of 27 levels,
909   which is the trace of the averaging kernel matrix and (INF) Shannon information content (in
910   bits), which includes information from the off-diagonal elements.   Of the four regions
911   considered in the plot, the MIPAS COF_2 retrieval is most sensitive in southern polar summer
912   with the combination of high concentrations and high stratospheric temperatures.

913

914   **Figure 6**. Vertical resolution as a function of altitude of the four retrievals shown in Figure
915   4.   The open squares show the vertical spacing of the retrieval grid (which is also the
916   measurement tangent height spacing) for the mid-latitude profile, for the other profiles the
917   pattern is the same but shifted up or down by a few kilometres.   The resolution at each
918   altitude is defined as the ratio of the diagonal of the averaging kernel matrix (Figure 5) to the
919   grid spacing, which is only meaningful where the averaging kernels have distinct peaks at the
920   tangent point. The MIPAS field-of-view is approximately 3 km high, which sets a practical
921   limit on the resolution obtainable at lower altitudes when the limb is oversampled.

922

923   **Figure 7**. ACE-FTS and MIPAS near-coincident individual profiles taken from the period
924   September 2009 to August 2010.   The locations and times of the eight observations can be
925   found in Table 6. The error bars represent the retrieval random errors. The plots also contain
926   the *a priori* profiles, and calculated SLIMCAT profiles for the location and time of each
927   ACE-FTS observation.

928

929   **Figure 8**. MIPAS and ACE zonal means between September 2009 and August 2010. The

930   plotted VMRs are the averages for each month of all filtered data at each altitude within 5˚

931   latitude bins. Note that the global coverage of the ACE-FTS observations between

932   September 2009 and August 2010 is poorer and noisier in appearance than MIPAS. A full

933   discussion of the seasonal variation in the COF_2 distribution is provided in the text.

934

935   **Figure 9**. A representative set of MIPAS and ACE individual latitude bins, with errors, taken

936   from Figure 8. SLIMCAT calculations are also included. A full discussion of the inter-

937   comparison is provided in the text.

938

939   **Figure 10**. Average loss rates (annual mean zonal mean; pptv/day) calculated by SLIMCAT

940   for COF_2 and its three main source gases, CFC-12, HCFC-22, and CFC-113. Full details of

941   the loss mechanisms are provided in the text.

942

943   **Figure 11**. A comparison between monthly SLIMCAT and ACE zonal means (September

944   2009 to August 2010). In order to reduce the noise and increase the latitude coverage for the

945   comparison, the plotted ACE data have been extended to the previous year. A full discussion

946   of the seasonal variation in the COF_2 distribution is provided in the text.

947

948   **Figure 12**. The MIPAS and SLIMCAT COF_2 time series between July 2002 and April 2012

949   for all latitudes at selected altitudes.

950

951   **Figure 13**. The ACE, MIPAS and SLIMCAT COF_2 time series between July 2002 and April

952   2012 for five altitude – latitude bin combinations.

953

954   **Figure 14**. Annual percentage trends (January 2004 to September 2010) for ACE, MIPAS,

955   and SLIMCAT as a function of latitude and altitude. A full discussion of these trends is

956   provided in the text.

957

958

959   **References**

960

961   Bernath, P. F., McElroy, C. T., Abrams, M. C., Boone, C. D., Butler, M., Camy-Peyret, C.,

962   Carleer, M., Clerbaux, C., Coheur, P.-F., Colin, R., DeCola, P., DeMazière, M., Drummond,

963   J. R., Dufour, D., Evans, W. F. J., Fast, H., Fussen, D., Gilbert, K., Jennings, D.E.,

964   Llewellyn, E. J., Lowe, R. P., Mahieu, E., McConnell, J. C., McHugh, M., McLeod, S. D.,

965   Michaud, R., Midwinter, C., Nassar, R., Nichitiu, F., Nowlan, C., Rinsland, C. P., Rochon, Y.

966   J., Rowlands, N., Semeniuk, K., Simon, P., Skelton, R., Sloan, J. J., Soucy, M.-A., Strong,

967   K., Tremblay, P., Turnbull, D., Walker, K. A., Walkty, I., Wardle, D. A., Wehrle, V., Zander,

968   R., and Zou, J.: Atmospheric Chemistry Experiment (ACE): Mission overview, Geophys.

969   Res. Lett., 32, L15S01, doi:10.1029/2005GL022386, 2005.

970

971   Boone, C. D., Walker, K. A., and Bernath, P. F.: Version 3 retrievals for the Atmospheric

972   Chemistry Experiment Fourier Transform Spectrometer (ACE-FTS), in: The Atmospheric

973   Chemistry Experiment ACE at 10: a Solar Occultation Anthology, edited by: Bernath, P. F.,

974   A.   Deepak   Publishing,   Hampton,   Virginia,   USA,   103–127,   available   at

975   http://acebox2.uwaterloo.ca/publications/2013/Version3.5retreivals2013.pdf (last access: 1

976   July 2014), 2013.

977

978   Brown, A. T., Chipperfield, M. P., Boone, C., Wilson, C., Walker, K. A., Bernath, P. F.:

979   Trends in atmospheric halogen containing gases since 2004, J. Quant. Spectrosc. Rad. Trans.,

980   112, 2552-2566, 2011.

981

982   Brown, A. T., Chipperfield, M. P., Richards, N. A. D., Boone, C., and Bernath, P. F.: Global

983   stratospheric fluorine inventory for 2004–2009 from Atmospheric Chemistry Experiment

984   Fourier Transform Spectrometer (ACE-FTS) measurements and SLIMCAT model

985   simulations, Atmos. Chem. Phys., 14, 267-282, doi:10.5194/acp-14-267-2014, 2014.

986

987   Chipperfield, M. P.: Multiannual simulations with a three-dimensional chemical transport

988   model, J. Geophys. Res., 104, 1781–1805, doi:10.1029/98jd02597, 1999.

989

990   Chipperfield, M. P.: New version of the TOMCAT/SLIMCAT off-line chemical transport

991   model: Intercomparison of stratospheric tracer experiments, Q. J. R. Meteorol. Soc., 132,

992   1179–1203, 2006.

993

994   Clerbaux, C., Coheur, P.-F., Hurtmans, D., Barret, B., Carleer, M., Colin, R., Semeniuk, K.,

995   McConnell, J. C., Boone, C., and Bernath, P.:, Carbon monoxide distribution from the ACE-

996 FTS solar occultation measurements, Geophys. Res. Lett., 32, L16S01,
997 doi:10.1029/2005GL022394, 2005.

998

999 Dhomse, S., Chipperfield, M. P., Feng, W., and Haigh, J. D.: Solar response in tropical
1000 stratospheric ozone: A 3-D chemical transport model study using ERA reanalyses, Atmos.
1001 Chem. Phys., 11, 12773-12786, doi:10.5194/acp-11-12773-2011, 2011.

1002

1003 Duchatelet, P., Mahieu, E., Ruhnke, R., Feng, W., Chipperfield, M., Demoulin, P., Bernath,
1004 P. F., Boone, C. D., Walker, K. A., Servais, C., and Flock, O.: An approach to retrieve
1005 information on the carbonyl fluoride (COF_2) vertical distributions above Jungfraujoch by
1006 FTIR multi-spectrum multi-window fitting, Atmos. Chem. Phys., 9, 9027–9042,
1007 doi:10.5194/acp-9-9027-2009, 2009.

1008

1009 Duchatelet, P., Demoulin, P., Hase, F., Ruhnke, R., Feng, W., Chipperfield, M. P., Bernath,
1010 P. F., Boone, C. D., Walker, K. A., and Mahieu, E.: Hydrogen fluoride total and partial
1011 column time series above the Jungfraujoch from long-term FTIR measurements: Impact of
1012 the line-shape model, characterization of the error budget and seasonal cycle, and comparison
1013 with satellite and model data, J. Geophys. Res., 115, D22306, doi:10.1029/2010JD014677,
1014 2010.

1015

1016 Feng, W., Chipperfield, M. P., Dorf, M., Pfeilsticker, K., and Ricaud, P.: Mid-latitude ozone
1017 changes: studies with a 3-D CTM forced by ERA-40 analyses, Atmos. Chem. Phys., 7, 2357–
1018 2369, doi:10.5194/acp-7-2357-2007, 2007.

1019

1020 Fischer, H., Birk, M., Blom, C., Carli, B., Carlotti, M., von Clarmann, T., Delbouille, L.,
1021 Dudhia, A., Ehhalt, D., Endemann, M., Flaud, J. M., Gessner, R., Kleinert, A., Koopman, R.,
1022 Langen, J., López-Puertas, M., Mosner, P., Nett, H., Oelhaf, H., Perron, G., Remedios, J.,
1023 Ridolfi, M., Stiller, G., and Zander, R.: MIPAS: an instrument for atmospheric and climate
1024 research, Atmos. Chem. Phys., 8, 2151-2188, doi:10.5194/acp-8-2151-2008, 2008.

1025

1026 Flaud, J.-M., Brizzi, G., Carlotti, M., Perrin, A., and Ridolfi, M.: MIPAS database:
1027 Validation of HNO_3 line parameters using MIPAS satellite measurements, Atmos. Chem.
1028 Phys., 6, 5037-5048, doi:10.5194/acp-6-5037-2006, 2006.

1029

1030   Gribble, G. W. Naturally Occurring Organofluorines. In Handbook of Environmental
1031   Chemistry, Vol.3, Part N: Organofluorines; Neilson, A. H., Ed.; Springer-Verlag: Berlin
1032   Heidelberg, 2002.

1033

1034   Harrison, J.J., and Bernath, P.F.: ACE-FTS observations of acetonitrile in the lower
1035   stratosphere, Atmos. Chem. Phys., 13, 7405-7413, doi:10.5194/acp-13-7405-2013, 2013.

1036

1037   Hartmann, J. M., Boulet, C., and Robert, D.: Collisional Effects on Molecular Spectra,
1038   Laboratory experiments and models, consequences for applications; Elsevier: Oxford, 2008.

1039

1040   Irion F.W., Gunson M.R., Toon G.C., Chang A.Y., Eldering A., Mahieu E., Manney G.L.,
1041   Michelsen H.A., Moyer E.J., Newchurch M.J., Osterman G.B., Rinsland C.P., Salawitch R.J.,
1042   Sen B., Yung Y.L., Zander R., Atmospheric Trace Molecule Spectroscopy (ATMOS)
1043   Experiment Version 3 data retrievals, Appl Opt. 2002 Nov 20;41(33):6968-79.

1044

1045   Kellmann, S., von Clarmann, T., Stiller, G. P., Eckert, E., Glatthor, N., Höpfner, M., Kiefer,
1046   M., Orphal, J., Funke, B., Grabowski, U., Linden, A., Dutton, G. S., and Elkins, J. W.: Global
1047   CFC-11 (CCl3F) and CFC-12 (CCl2F2) measurements with the Michelson Interferometer for
1048   Passive Atmospheric Sounding (MIPAS): retrieval, climatologies and trends, Atmos. Chem.
1049   Phys., 12, 11857-11875, doi:10.5194/acp-12-11857-2012, 2012.

1050

1051   May, R. D.: Line intensities and collisional-broadening parameters for the v_4 and v_6 bands of
1052   carbonyl fluoride, J. Quant. Spectrosc. Radiat. Transfer, 48, 701–712, 1992.

1053

1054   Mélen, F., Mahieu, E., Zander, R., Rinsland, C. P., Demoulin, P., Roland, G., Delbouille, L.,
1055   and Servais, C.: Vertical column abundances of COF_2 above the Jungfraujoch Station,
1056   derived from ground-based infrared solar observations, J. Atmos. Chem., 29, 119–134, 1998.

1057

1058   Monge-Sanz, B. M., Chipperfield, M. P., Simmons, A. J., and Uppala, S. M.: Mean age of air
1059   and transport in a CTM: Comparison of different ECMWF analyses, Geophys. Res. Lett., 34,
1060   L04801, doi:10.1029/2006gl028515, 2007.

1061

1062   Plumb, R. A. and Ko, M. K. W.: Interrelationships between mixing ratios of long-lived
1063   stratospheric constituents, J. Geophys. Res., 97, 10145–10156, 1992.

1064

1065 Remedios, J. J., Leigh, R. J., Waterfall, A. M., Moore, D. P., Sembhi, H., Parkes, I.,
1066 Greenhough, J., Chipperfield, M.P., and Hauglustaine, D.: MIPAS reference atmospheres and
1067 comparisons to V4.61/V4.62 MIPAS level 2 geophysical data sets, Atmos. Chem. Phys.
1068 Discuss., 7, 9973–10017, doi:10.5194/acpd-7-9973-2007, 2007

1069

1070 Ricaud, P. and Lefevre, F.: Fluorine in the atmosphere, in: Fluorine and the Environment:
1071 Atmospheric Chemistry, Emissions, & Lithosphere, edited by: Tressaud, A., Elsevier,
1072 Oxford, UK, 2006.

1073

1074 Rinsland, C. P., Zander, R., Brown, L. R., Farmer, C. B., Park, J. H., Norton, R. H., Russell,
1075 III, J. M., and Raper, O. F.: Detection of carbonyl fluoride in the stratosphere, Geophys. Res.
1076 Lett., 13, 769–772, 1986.

1077

1078 Rodgers, C. D.: Inverse methods for atmospheric sounding: Theory and Practice, Volume 2
1079 of Series on Atmospheric, Oceanic and Planetary Physics, World Scientific Co. Pte. Ltd.,
1080 Singapore, 2000.

1081

1082 Rothman, L., Jacquemart, D., Barbe, A., Benner, C. D., Birk, M., Brown, L. R., Carleer, M.
1083 R., Chackerian Jr., C., Chance, K., Coudert, L. H., Dana, V., Devi, V. M., Flaud, J.-M.,
1084 Gamache, R. R., Goldman, A., Hartmann, J.-M., Jucks, J. W., Maki, A. G., Mandin, J.-Y.,
1085 Massie, S. T., Orphal, J., Perrin, A., Rinsland, C. P., Smith, M., Tennyson, J., Tolchenov, R.
1086 N., Toth, R. A., Vander Auwera, J., Varanasi, P., and Wagner, G.: The HITRAN 2004
1087 molecular spectroscopic database, J. Quant. Spectrosc. Radiat. Transfer, 96, 193–204, 2005.

1088

1089 Sharpe S. W., Johnson T. J., Sams R. L., Chu P. M., Rhoderick G. C., and Johnson P. A.:
1090 Gas-phase databases for quantitative infrared spectroscopy, Appl Spectrosc. 2004;58:1452-
1091 61.

1092

1093 Spang, R., Remedios, J. J., and Barkley, M.: Colour indices for the detection and
1094 differentiation of cloud types in infra-red limb emission spectra, Adv. Space Res., 33, 1041–
1095 1047, 2004.

1096

1097   Stiller, G. P., von Clarmann, T., Haenel, F., Funke, B., Glatthor, N., Grabowski, U.,

1098   Kellmann, S., Kiefer, M., Linden, A., Lossow, S., and López-Puertas, M.: Observed temporal

1099   evolution of global mean age of stratospheric air for the 2002 to 2010 period, Atmos. Chem.

1100   Phys., 12, 3311-3331, doi:10.5194/acp-12-3311-2012, 2012.

1101

1102   Toon, G. C., personal communication, 2012.

1103

1104   Velazco, V. A., Toon, G. C., Blavier, J.-F. L., Kleinböhl, A., Manney, G. L., Daffer, W. H.,

1105   Bernath, P. F., Walker, K. A., and Boone, C.: Validation of the Atmospheric Chemistry

1106   Experiment by noncoincident MkIV balloon profiles, J. Geophys. Res., 116, D06306,

1107   doi:10.1029/2010jd014928, 2011.

1108

1109   von Clarmann, T.: Smoothing error pitfalls, Atmos. Meas. Tech. Discuss., 7, 3301-3319,

1110   doi:10.5194/amtd-7-3301-2014, 2014 (current status: Atmos. Meas. Tech. in press).

1111

1112   WMO/UNEP: Scientific Assessment of Ozone Depletion: 2010, Global Ozone Research and

1113   Monitoring Project-Report No. 52, 516 pp., Geneva, Switzerland, 2011.

1114

1115   Zander, R., Rinsland, C. P., Mahieu, E., Gunson, M. R., Farmer, C. B., Abrams, M. C., and

1116   Ko, M. K. W.: Increase of carbonyl fluoride (COF_2) in the stratosphere and its contribution to

1117   the 1992 budget of inorganic fluorine in the upper stratosphere, J. Geophys. Res., 99, 16737–

1118   16743, 1994.

1119

Tables

Table 1: Microwindows for the v3.0 ACE-FTS carbonyl fluoride retrieval.

Centre Frequency (cm^{-1})	Microwindow width (cm^{-1})	Lower altitude (km)	Upper altitude (km)
1234.70	1.40	12	$45-11\sin^2$(latitude°)
1236.90	1.40	25	$45-11\sin^2$(latitude°)
1238.00	0.80	15	$45-11\sin^2$(latitude°)
1239.90	1.00	15	$45-11\sin^2$(latitude°)
1930.60	1.40	$15-3\sin^2$(latitude°)	$45-11\sin^2$(latitude°)
1936.48	0.65	12	$45-11\sin^2$(latitude°)
1938.15	1.50	30	$35-6\sin^2$(latitude°)
1939.55	1.20	30	$35-6\sin^2$(latitude°)
1949.40	1.20	15	$45-11\sin^2$(latitude°)
1950.70	0.50	12	$45-11\sin^2$(latitude°)
1952.23	1.00	12	$45-11\sin^2$(latitude°)
2672.70[a]	0.60	12	20

[a] Included to improve results for interferer HDO.

Table 2: Interferers in the v3.0 ACE-FTS carbonyl fluoride retrieval.

Molecule	Lower altitude limit (km)	Upper altitude limit (km)
H_2O	12	$45-11\sin^2$(latitude°)
CO_2	12	$45-11\sin^2$(latitude°)
CH_4	12	$45-11\sin^2$(latitude°)
NO	12	$45-11\sin^2$(latitude°)
$^{13}CH_4$	12	$45-11\sin^2$(latitude°)
$OC^{18}O$	12	$45-11\sin^2$(latitude°)
N_2O	12	$45-11\sin^2$(latitude°)
$N_2^{18}O$	12	$32-2\sin^2$(latitude°)
^{15}NNO	12	$27-2\sin^2$(latitude°)
HDO	12	24
CH_3D	12	23

1128   Table 3: Microwindows for the MIPAS carbonyl fluoride retrieval.

Centre Frequency (cm^{-1})	Microwindow width (cm^{-1})	Lower altitude (km)	Upper altitude (km)
773.5000	3.0000	18.0	43.0
1223.9375	3.0000	10.5	54.0
1227.21875	2.9375	16.5	46.0
1231.8750	3.0000	12.0	40.0
1234.7500	2.1250	7.5	19.5

1129

1130   Table 4: Interferers in the MIPAS carbonyl fluoride retrieval.

Molecule	Lower altitude limit (km)	Upper altitude limit (km)
H_2O	7.5	54.0
CO_2	7.5	54.0
O_3	7.5	54.0
N_2O	7.5	54.0
CH_4	7.5	54.0
NO_2	18.0	43.0
HNO_3	10.5	54.0
NH_3	18.0	43.0
$HOCl$	7.5	54.0
HCN	18.0	43.0
H_2O_2	7.5	54.0
CCl_4	18.0	43.0
$ClONO_2$	18.0	43.0
N_2O_5	7.5	46.0

1131

1132   Table 5: Sources of systematic uncertainty in the ACE-FTS v3.0 carbonyl fluoride retrieval.

Source	Symbol	Fractional value
COF_2 spectroscopy	μ_{spec}	0.15
Spectral interferers	μ_{int}	0.01
Temperature	μ_T	0.04
Altitude	μ_z	0.04
ILS	μ_{ILS}	0.01

1133

1134

1135   Table 6: Near-coincident ACE-FTS and MIPAS measurements.

Date	ACE-FTS				MIPAS			
	Occ	Time (UTC)	Lat	long	Orbit	Time (UTC)	Lat	Long
3-1-2010	sr34426	13:22:21	54.78	-72.91	41018	15:10:28	54.71	-72.95
4-2-2010	sr34898	13:53:50	67.27	-71.25	41476	15:01:10	67.19	-70.93
25-5-2010	sr36514	04:27:21	68.86	-59.05	43043	02:06:49	68.60	-59.45
10-7-2010	sr37203	23:03:33	-59.27	-211.3	43714	23:56:31	-59.16	-210.87

1136

sr11613
28.9 km
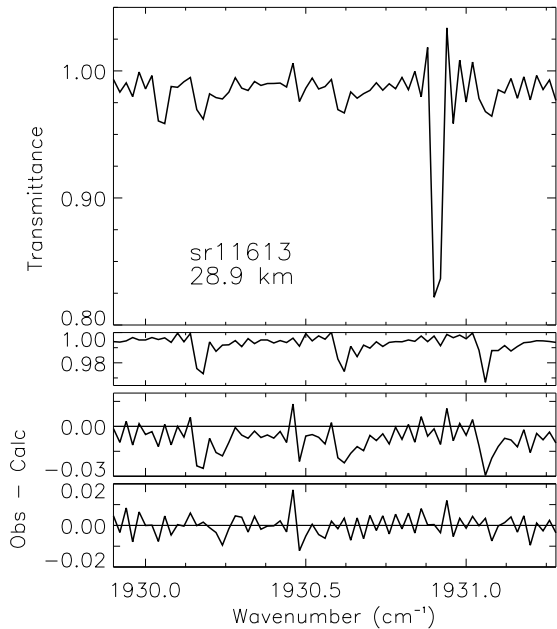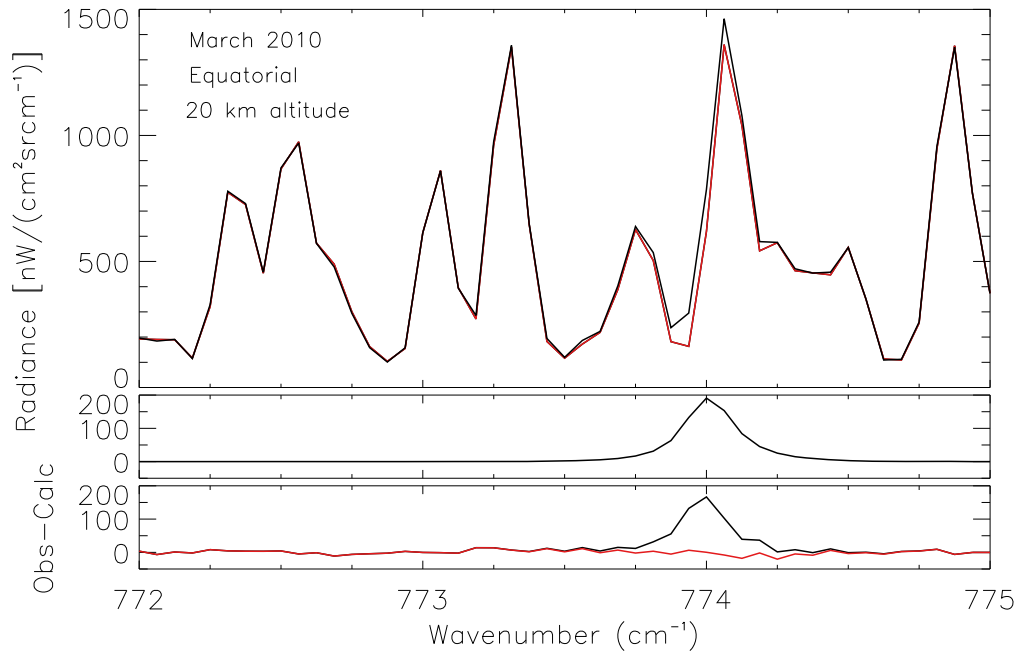
MIPAS COF$_2$ OR27 Day Error

MIPAS COF$_2$ Profiles

NPW
MID
EQU
SPS

Altitude [km]

VMR [pptv]

MIPAS 09/2009 ACE 09/2009 MIPAS 10/2009 ACE 10/2009 MIPAS 11/2009 ACE 11/2009

MIPAS 12/2009 ACE 12/2009 MIPAS 01/2010 ACE 01/2010 MIPAS 02/2010 ACE 02/2010

MIPAS 03/2010 ACE 03/2010 MIPAS 04/2010 ACE 04/2010 MIPAS 05/2010 ACE 05/2010

MIPAS 06/2010 ACE 06/2010 MIPAS 07/2010 ACE 07/2010 MIPAS 08/2010 ACE 08/2010

COF_2 (ppt)

0   44   88   132   176   220   264   308   352   396
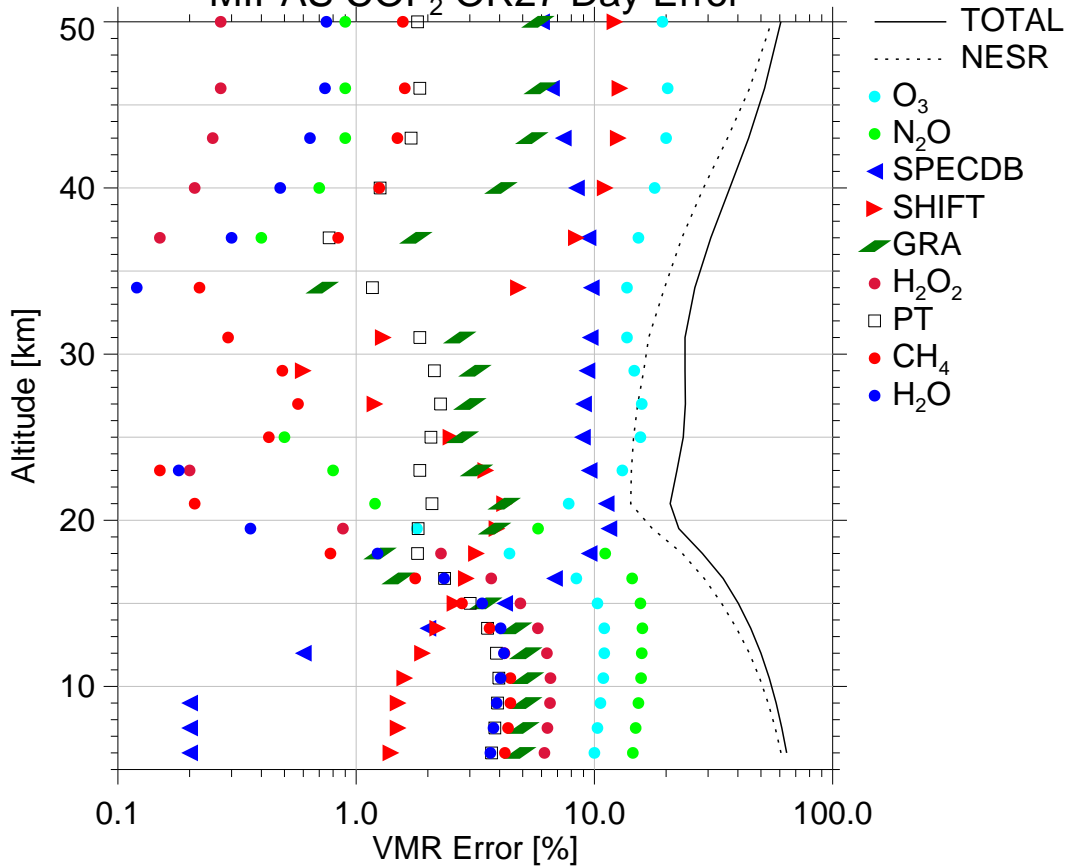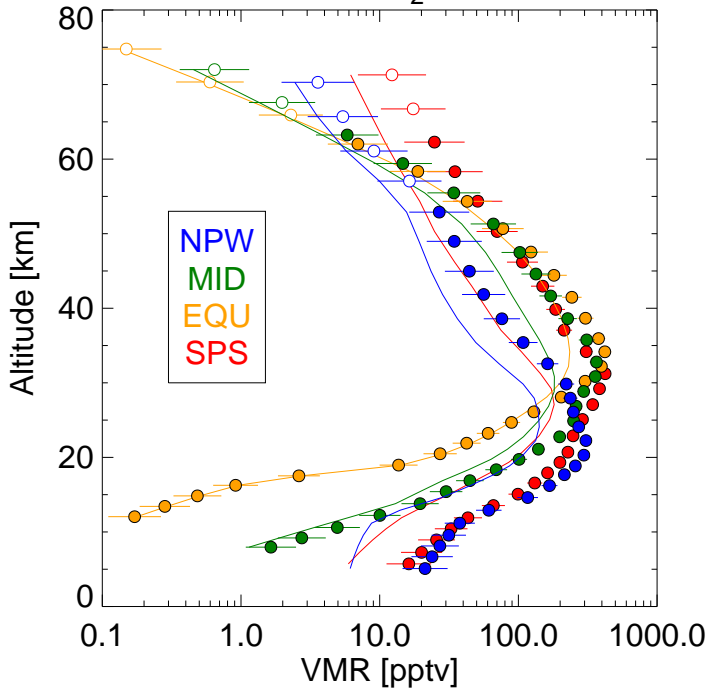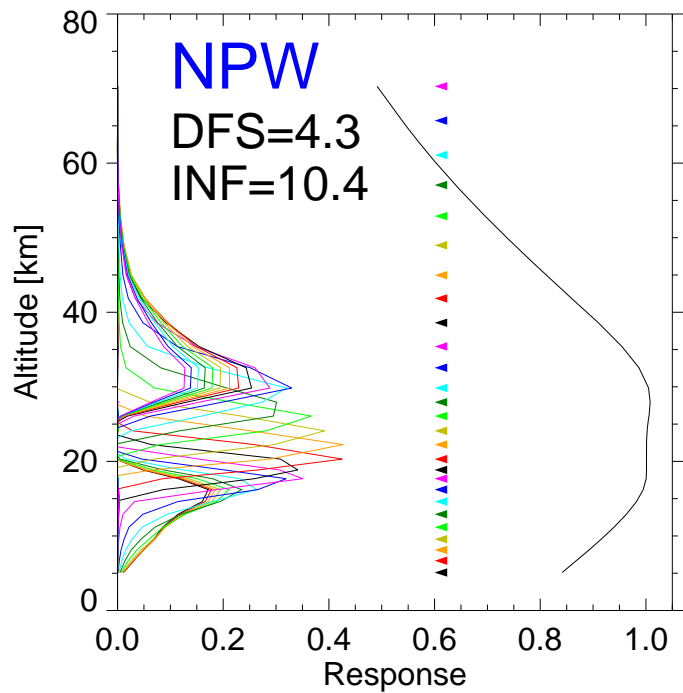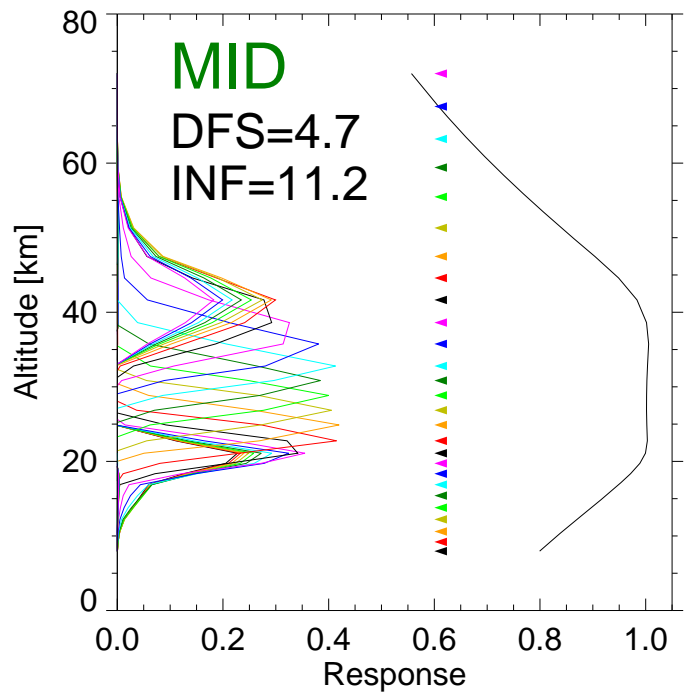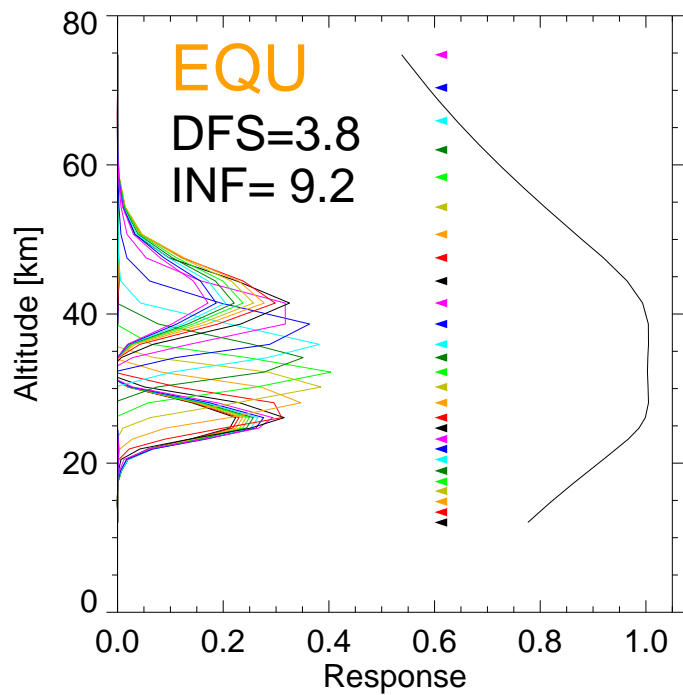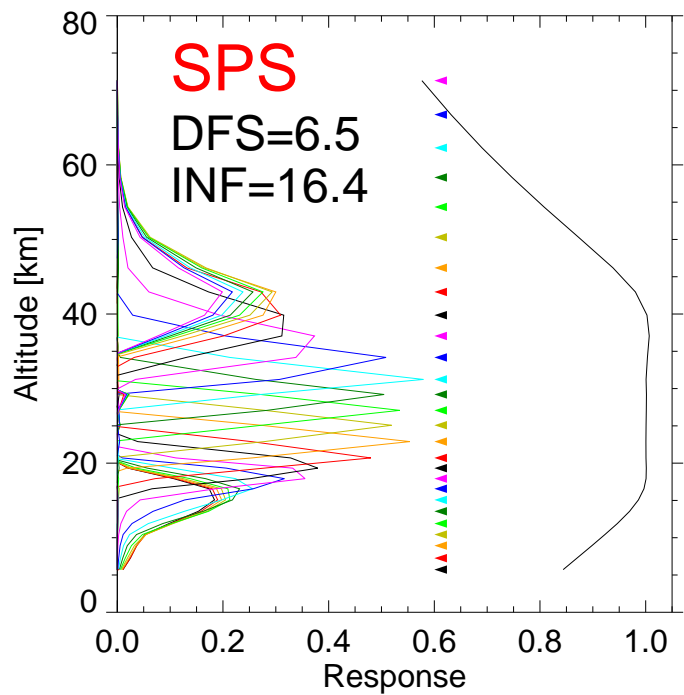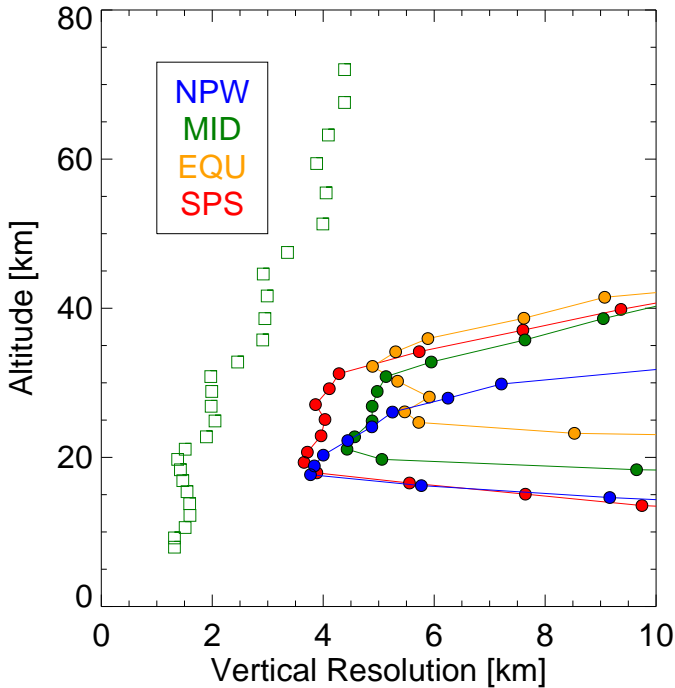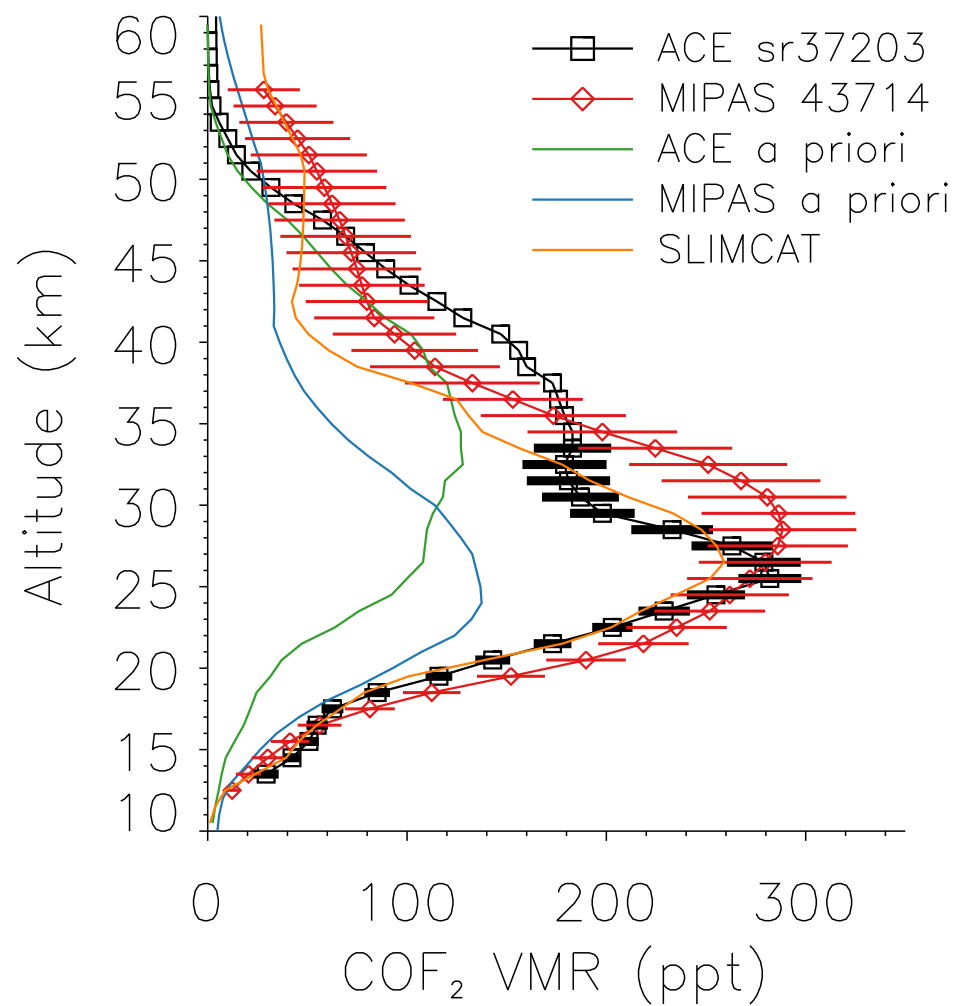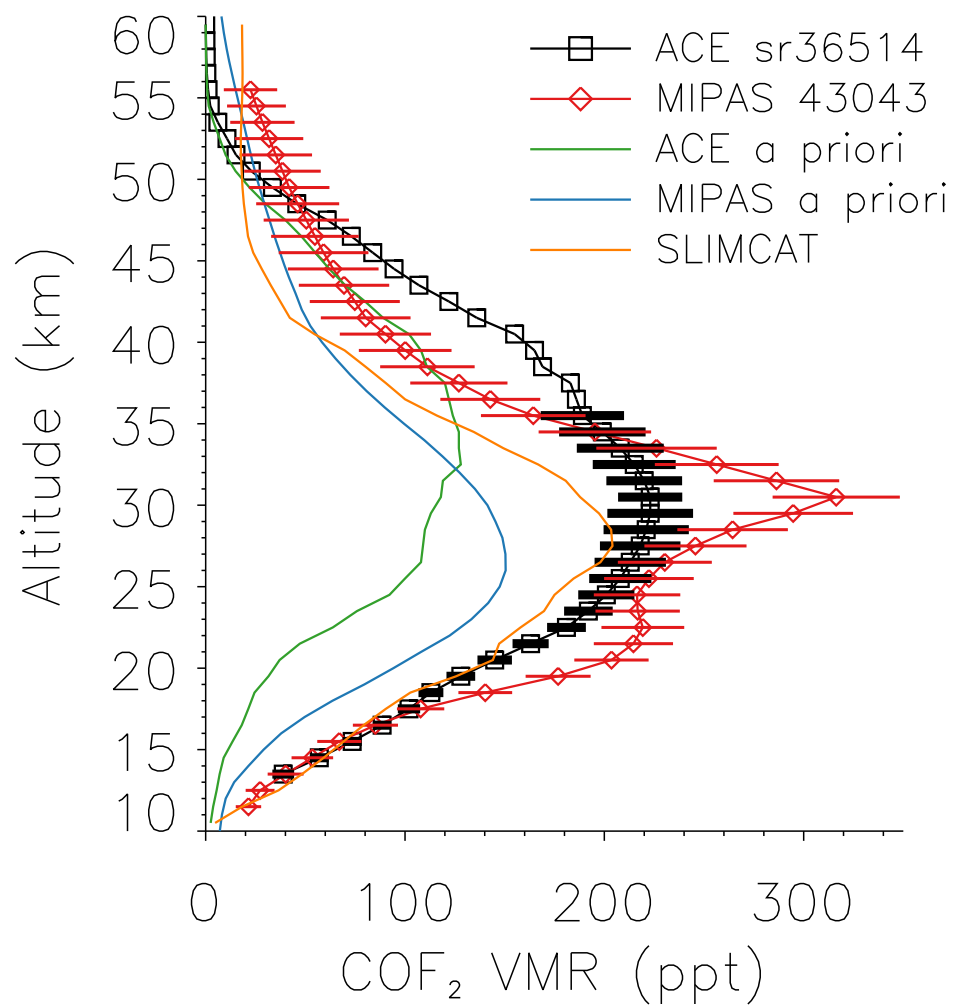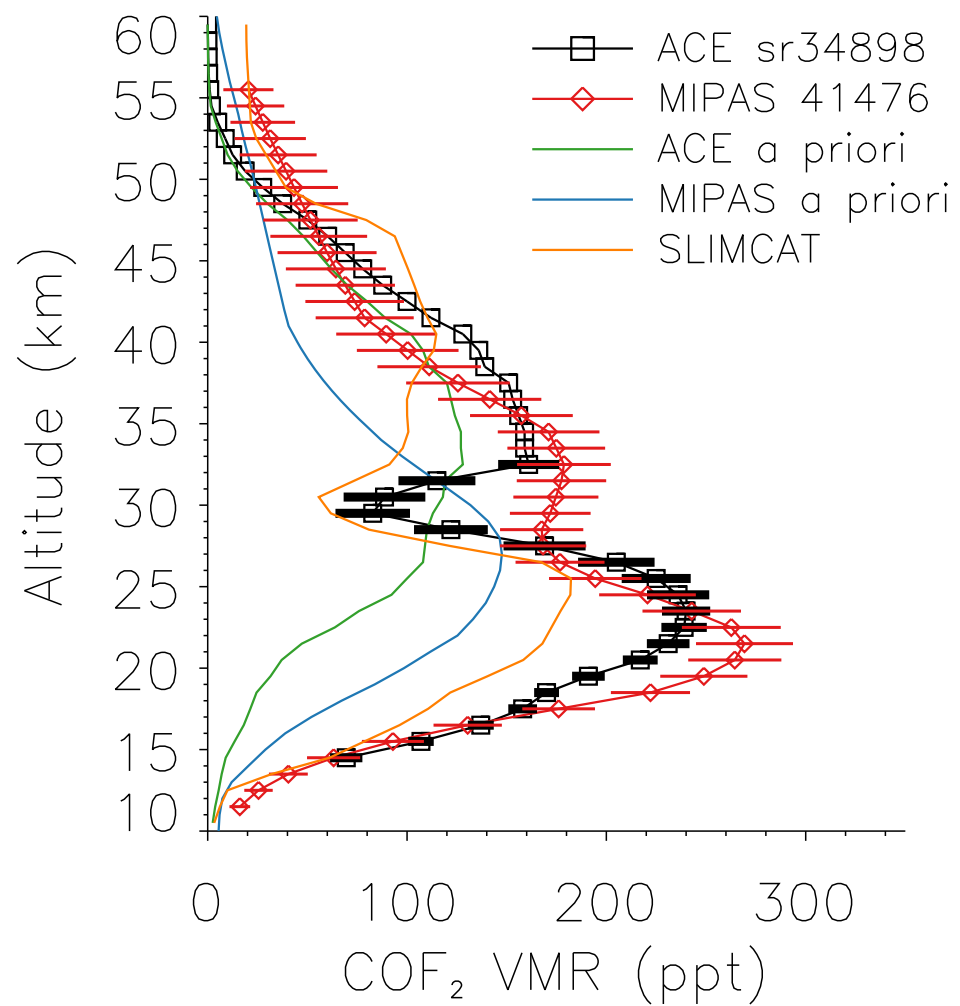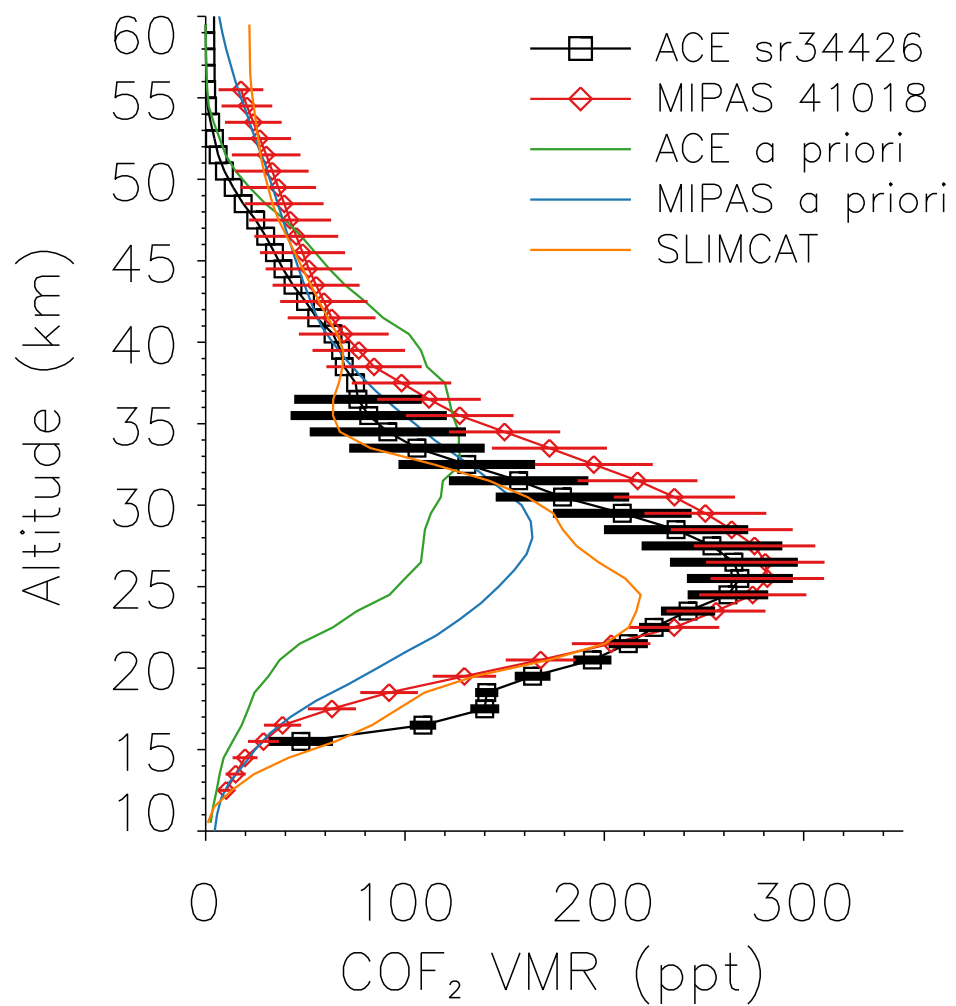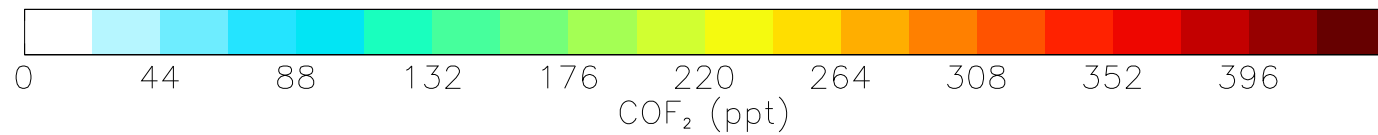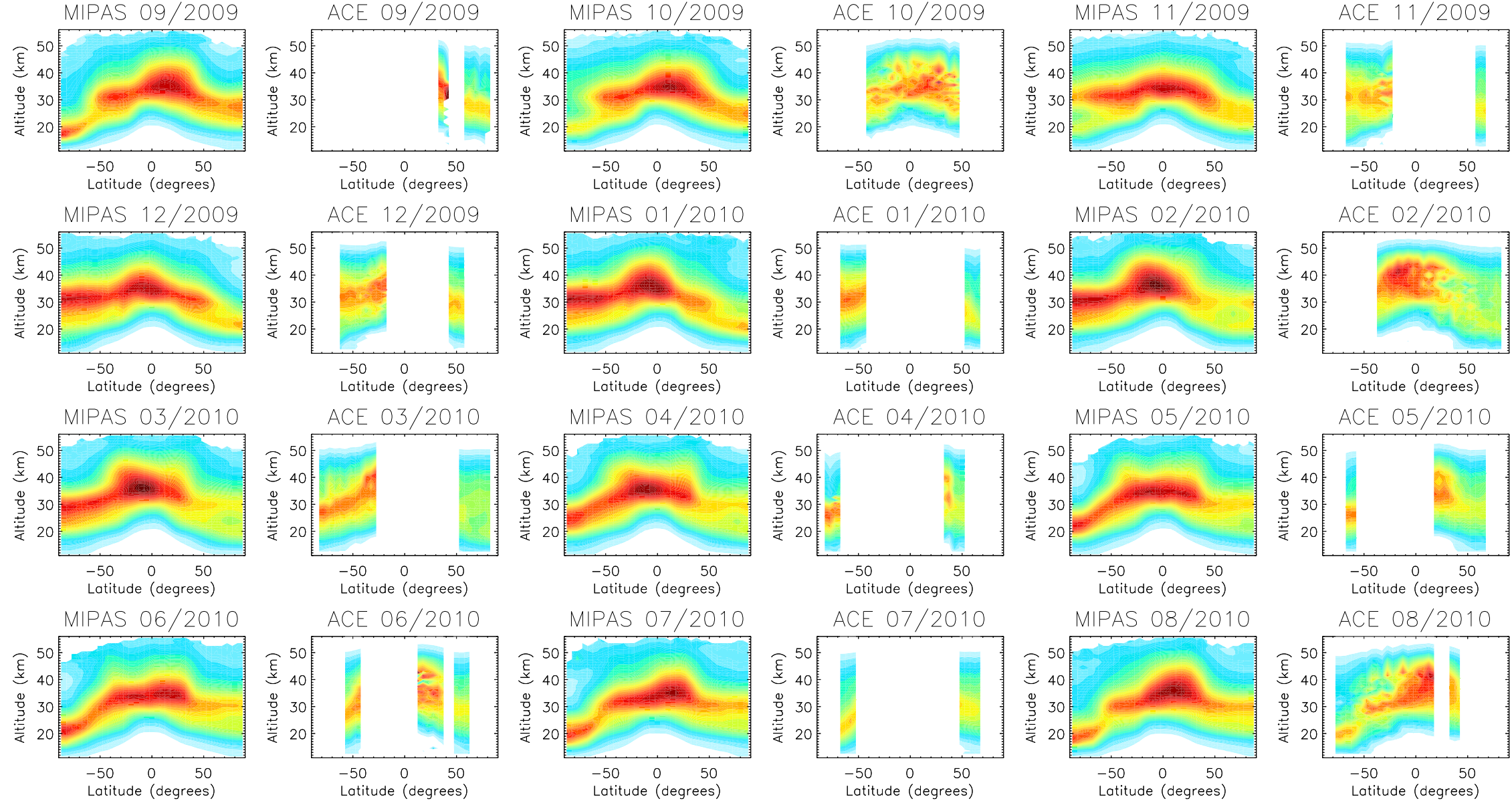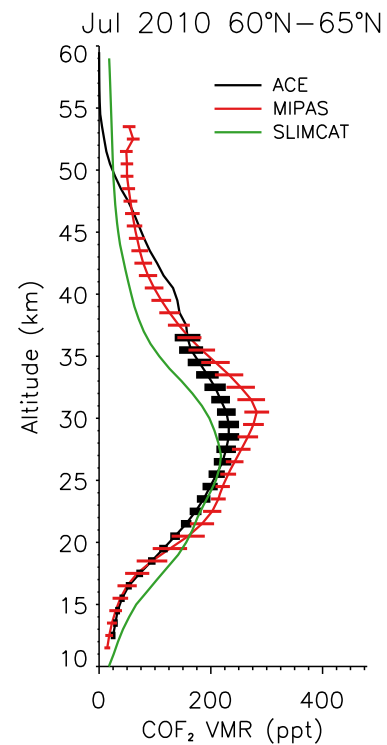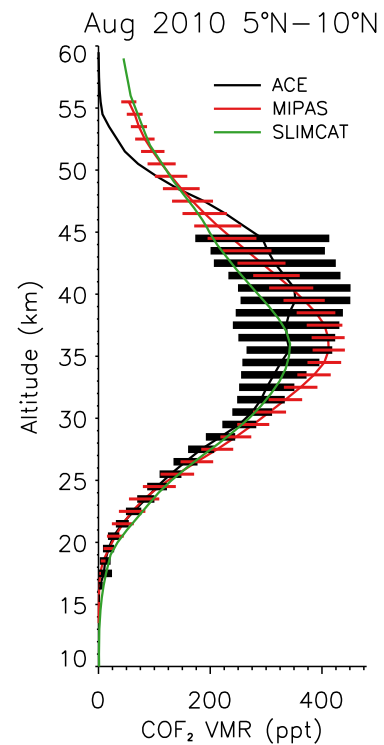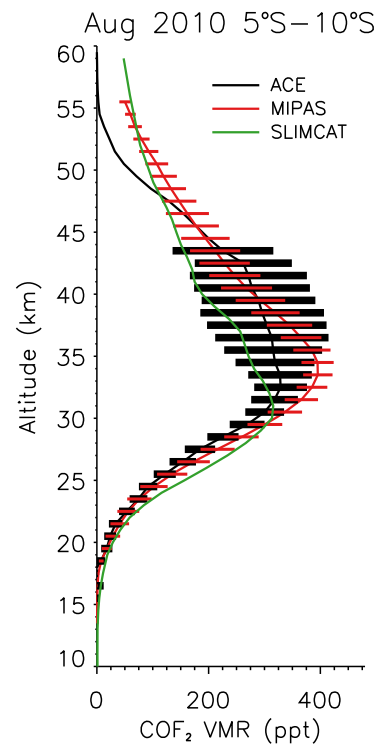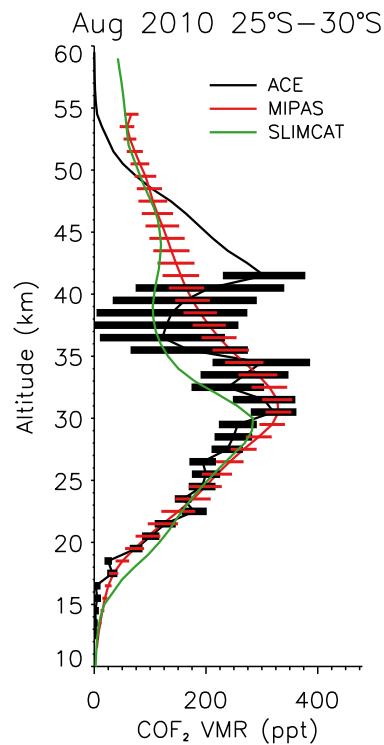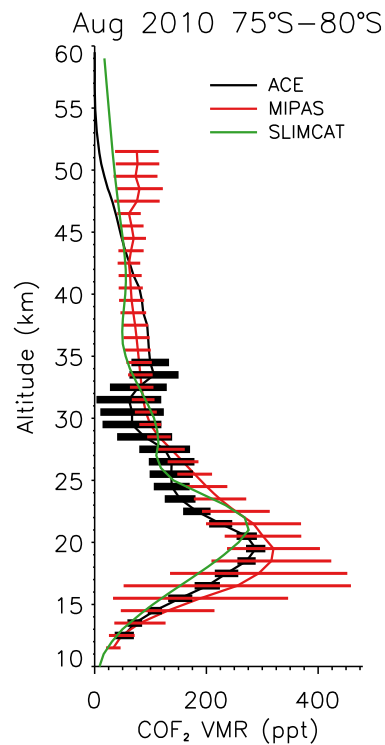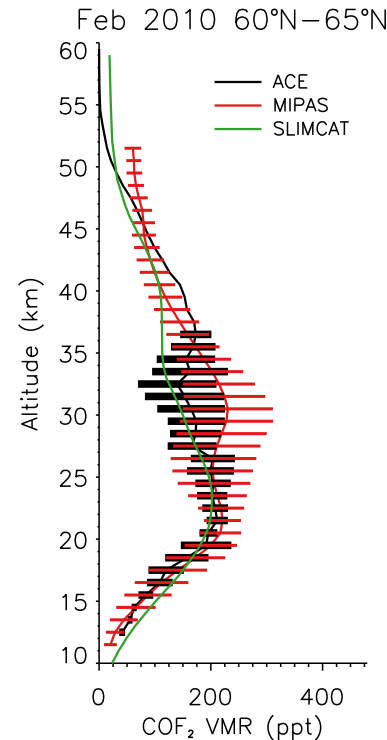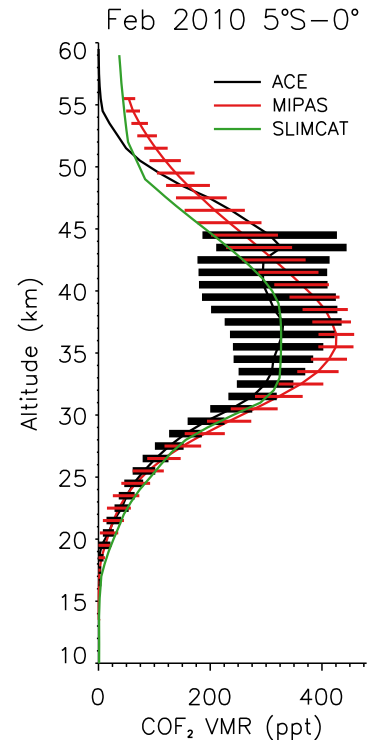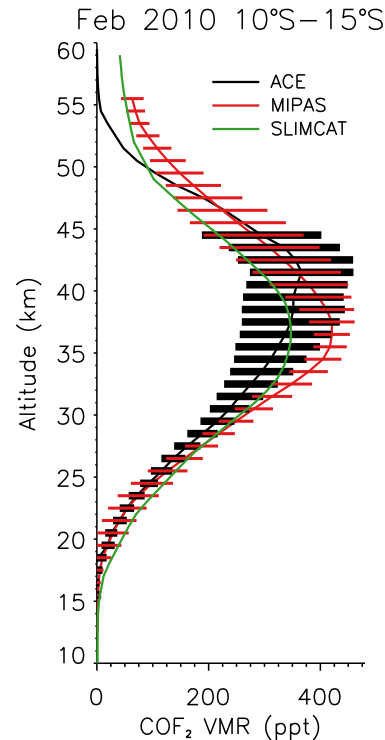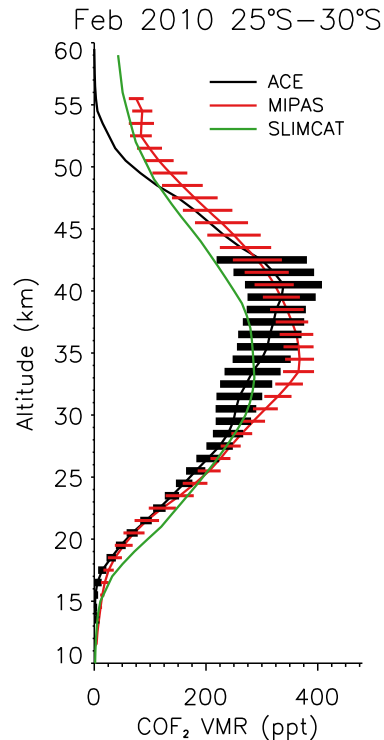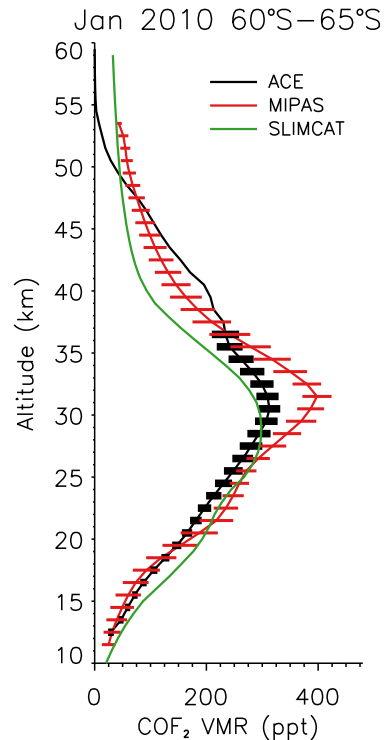
CFC−12 loss rate (pptv/day)
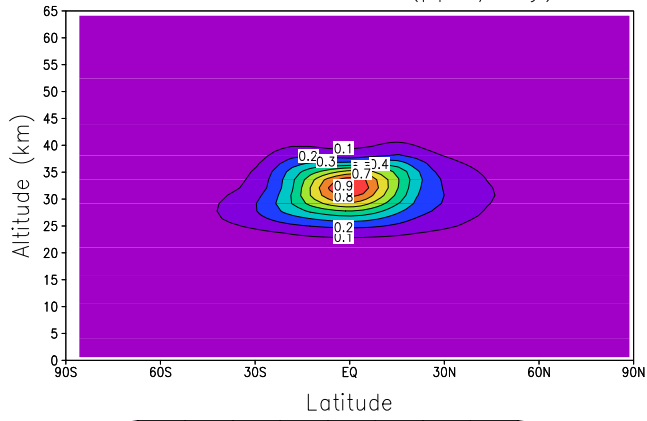
HCFC−22 loss rate (pptv/day)
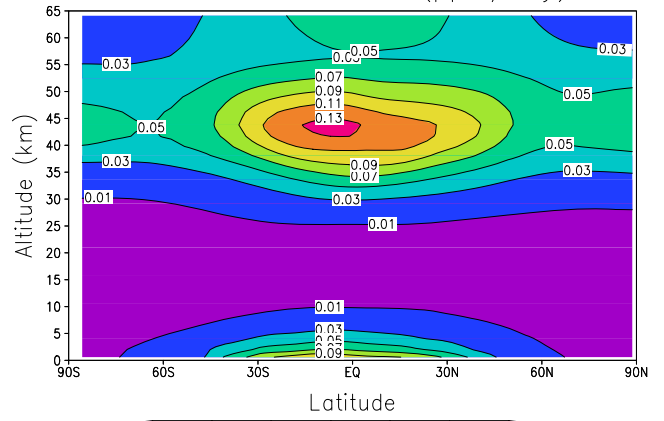
CFC−113 loss rate (pptv/day)

COF2 loss rate (pptv/day)

SLIMCAT 09/2009 · ACE 09/2008&09 · SLIMCAT 10/2009 · ACE 10/2008&09 · SLIMCAT 11/2009 · ACE 11/2008&09 · SLIMCAT 12/2009 · ACE 12/2008&09 · SLIMCAT 01/2010 · ACE 01/2009&10 · SLIMCAT 02/2010 · ACE 02/2009&10 · SLIMCAT 03/2010 · ACE 03/2009&10 · SLIMCAT 04/2010 · ACE 04/2009&10 · SLIMCAT 05/2010 · ACE 05/2009&10 · SLIMCAT 06/2010 · ACE 06/2009&10 · SLIMCAT 07/2010 · ACE 07/2009&10 · SLIMCAT 08/2010 · ACE 08/2009&10

Altitude (km) · Latitude (degrees)

COF_2 (ppt)

0   44   88   132   176   220   264   308   352   396

MIPAS: 20.5 km   SLIMCAT: 20.5 km
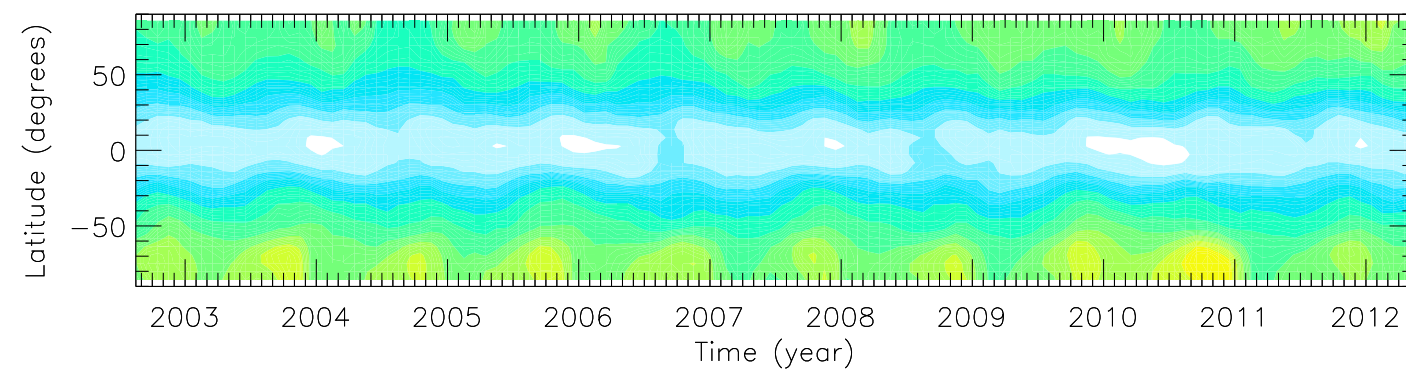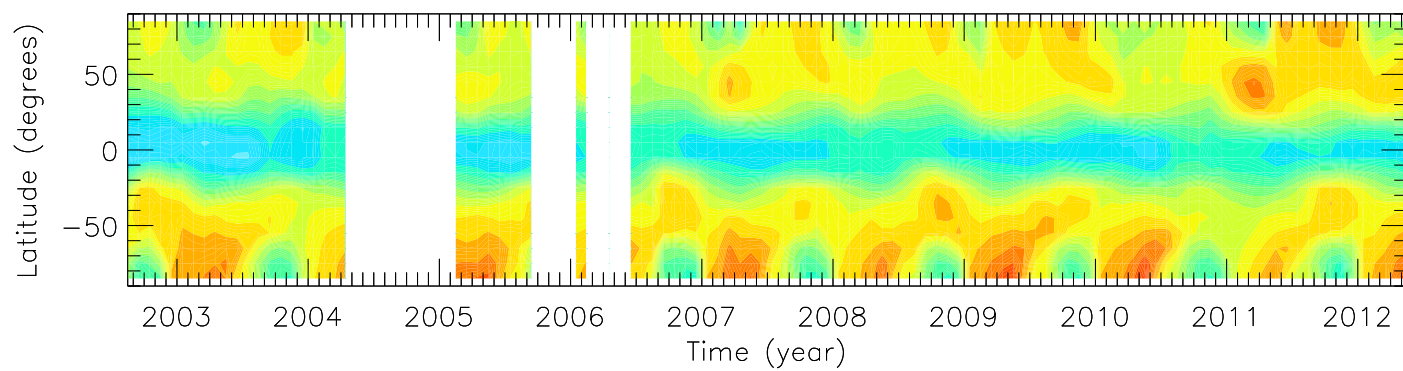
MIPAS: 25.5 km   SLIMCAT: 25.5 km
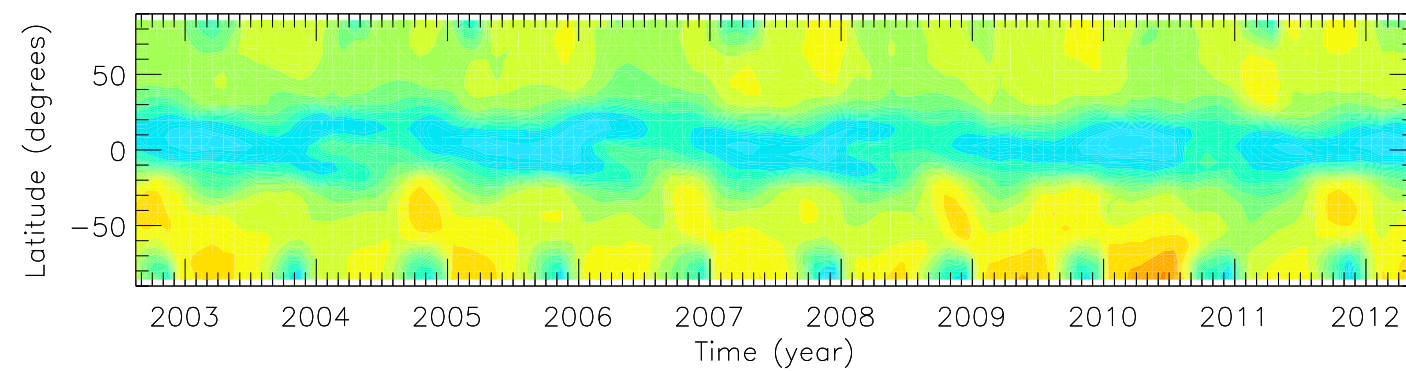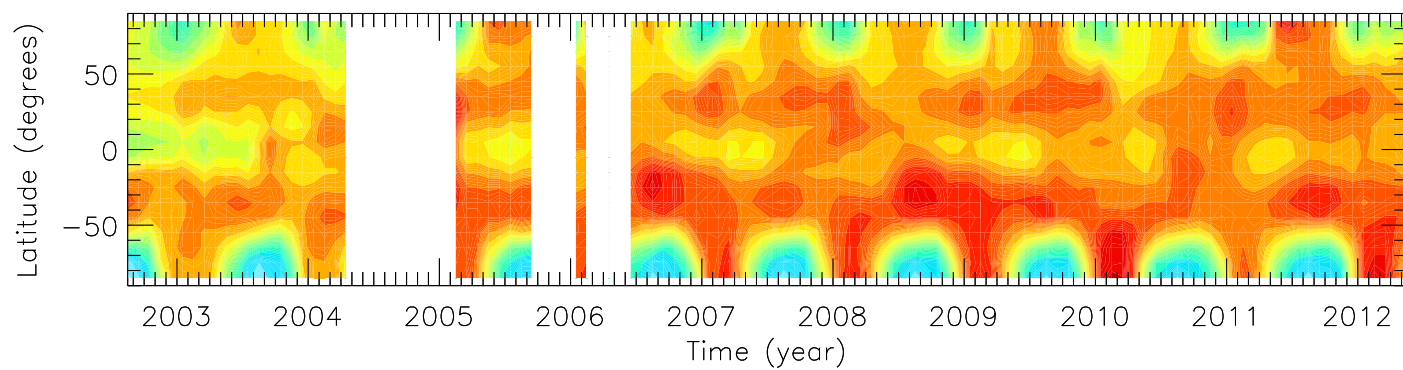
MIPAS: 30.5 km   SLIMCAT: 30.5 km
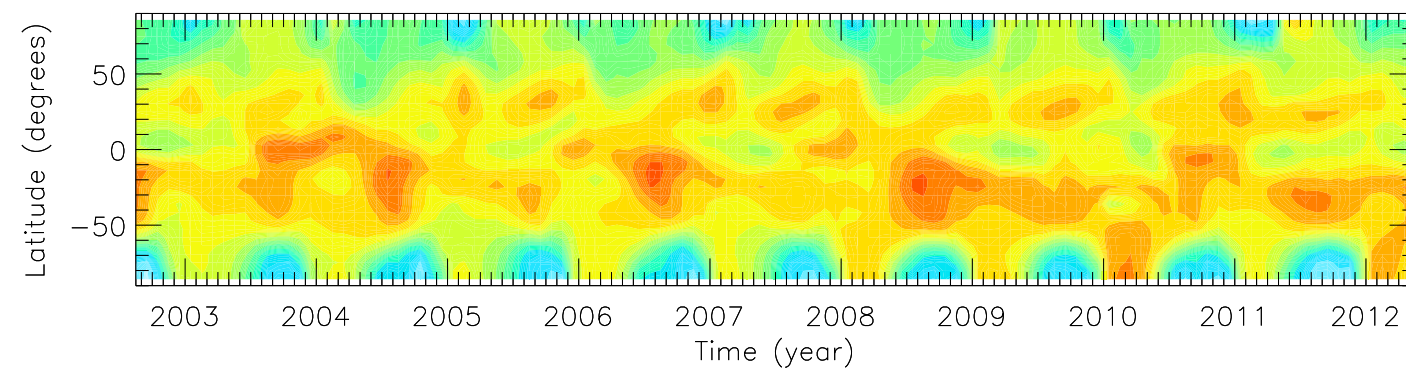
MIPAS: 35.5 km   SLIMCAT: 35.5 km
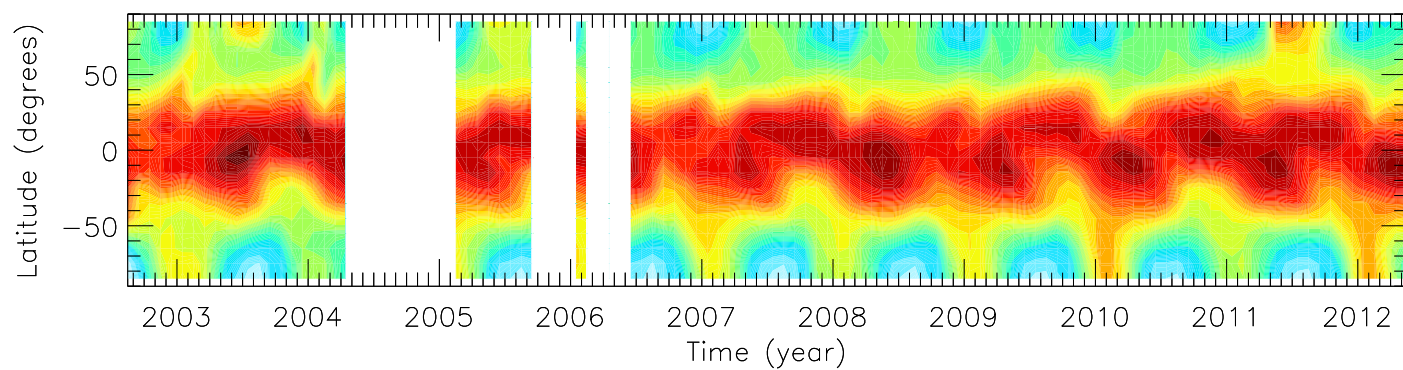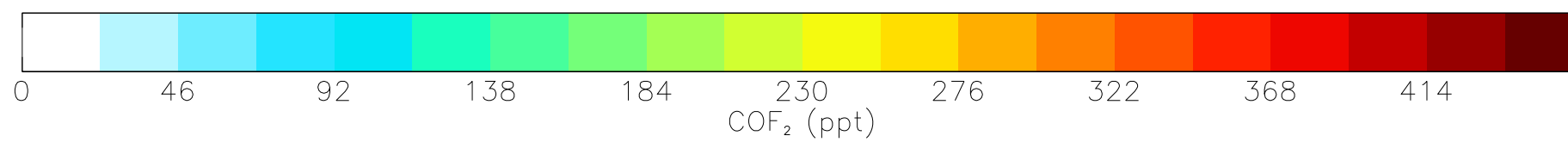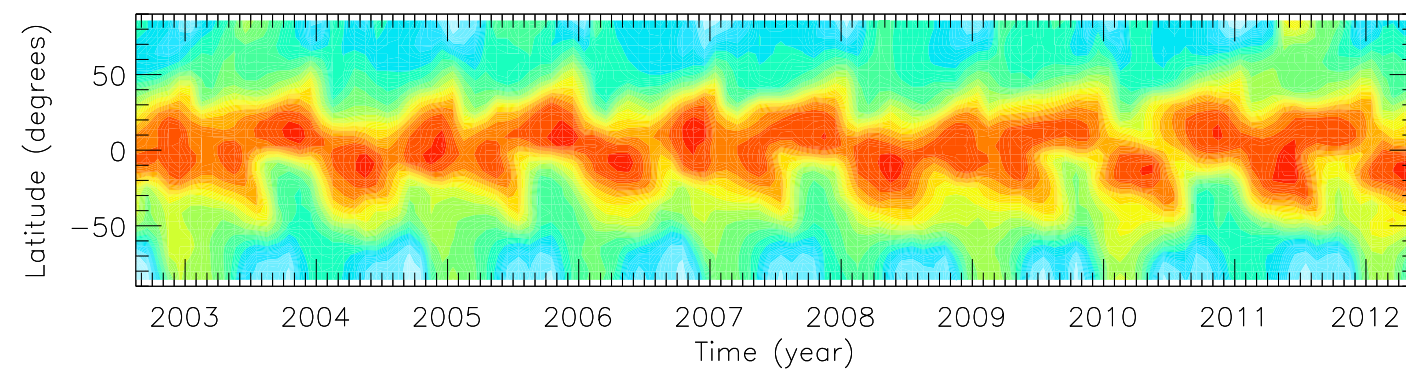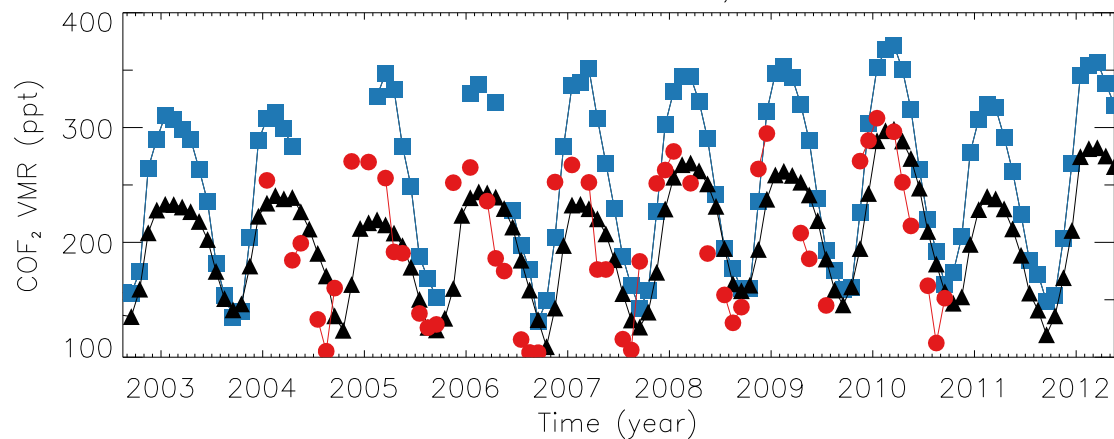
COF_2 (ppt)

0   46   92   138   184   230   276   322   368   414
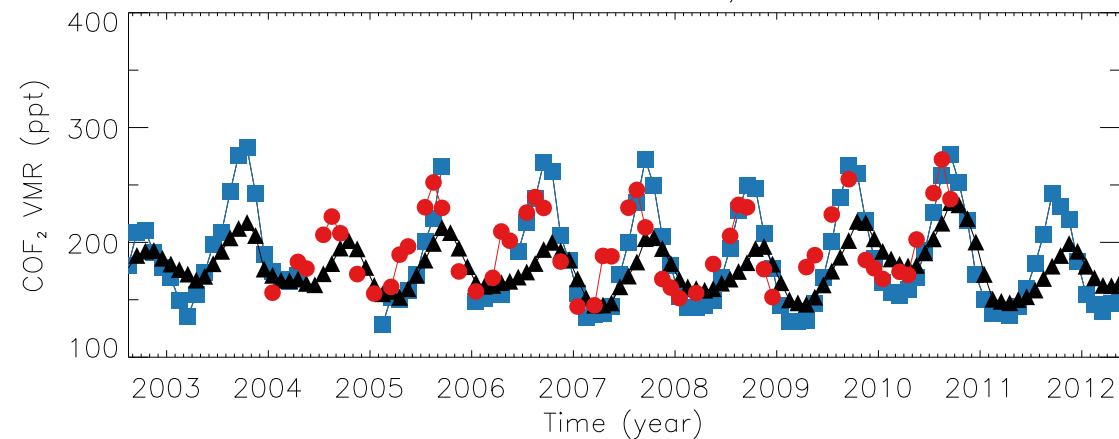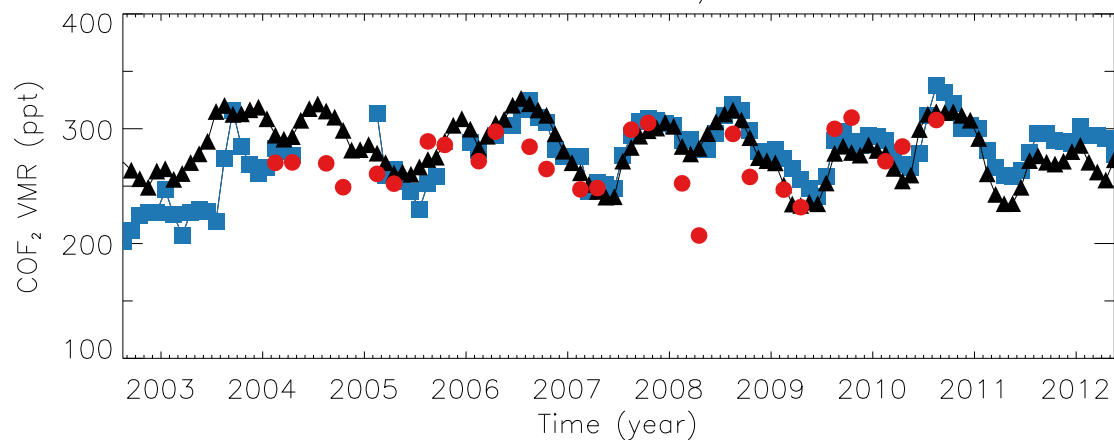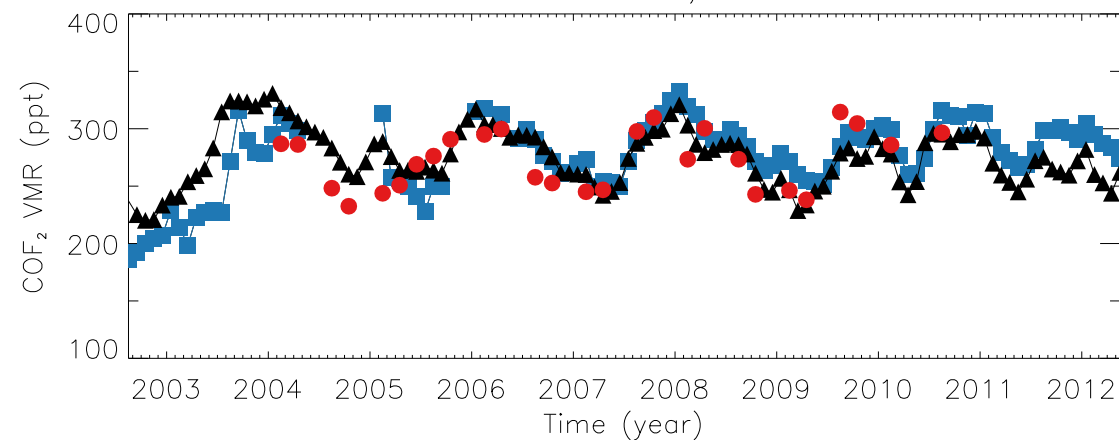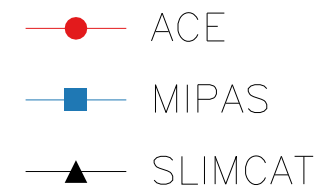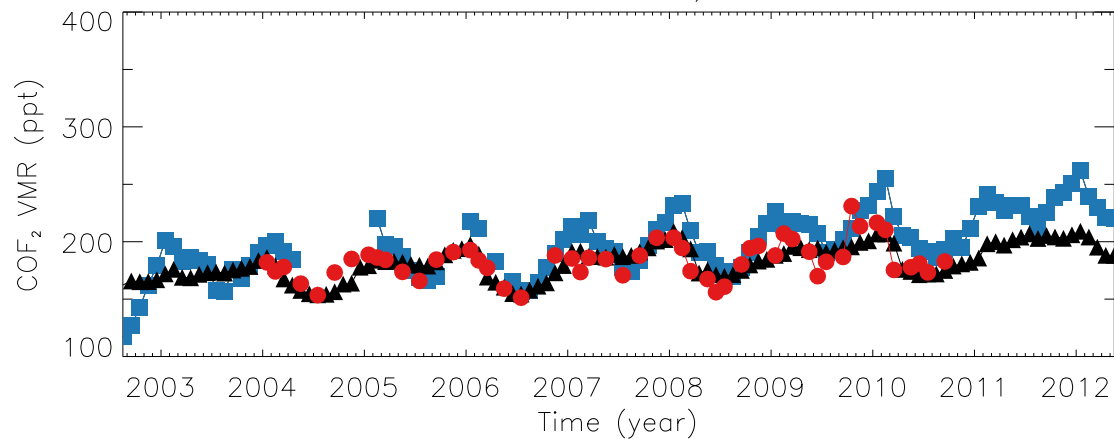
MIPAS COF$_2$ trends (January 2004 to September 2010)
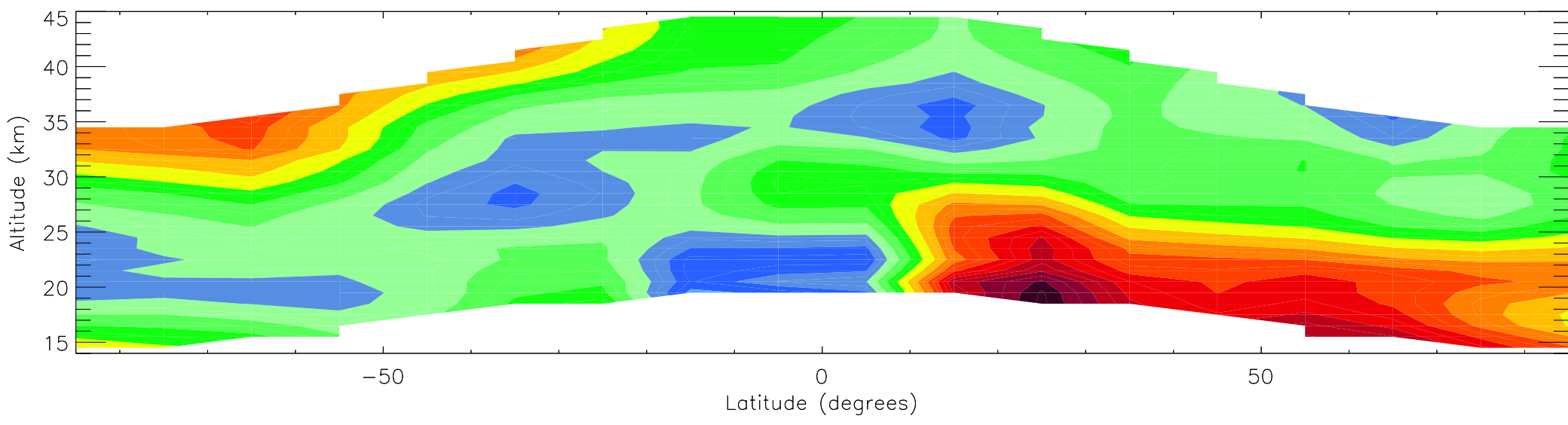
ACE COF$_2$ trends (January 2004 to September 2010)
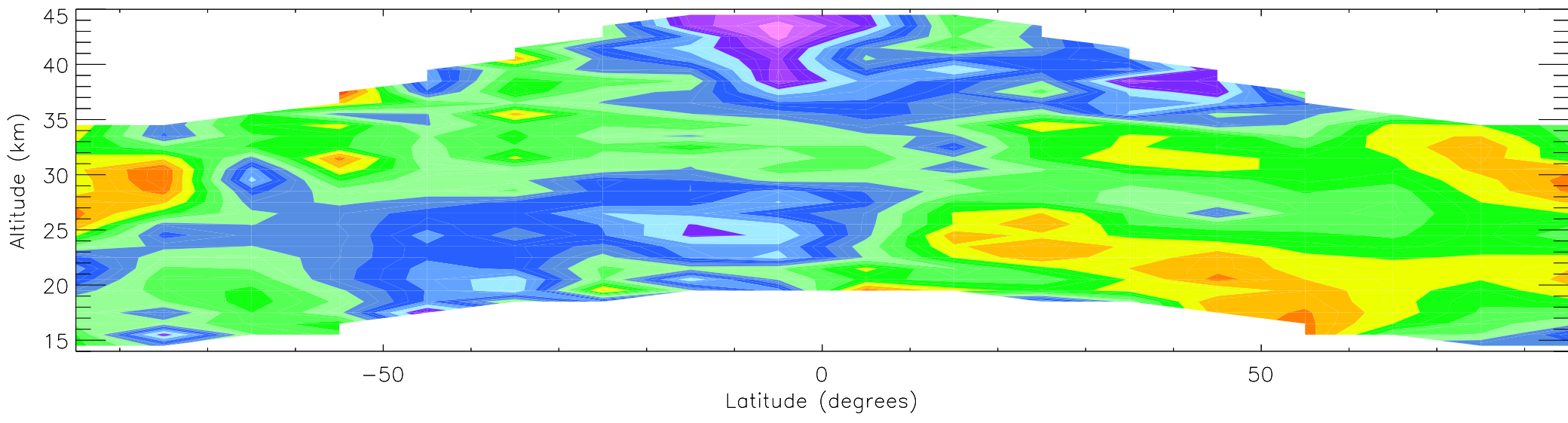
SLIMCAT COF$_2$ trends (January 2004 to September 2010)
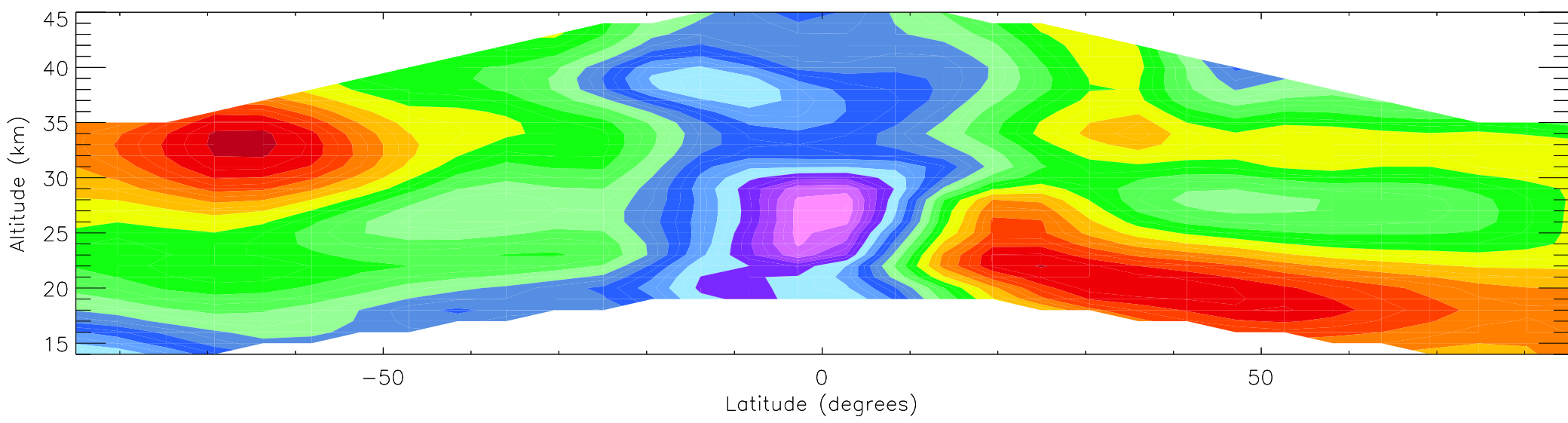
SLIMCAT COF$_2$ trends (January 2004 to September 2010) – fixed to 2000 dynamics